ADVANCED FUNCTIONAL MATERIALS
www.afm-journal.de

Unraveling Dual Mechanisms in Quasi-Layered Bi_2O_2Se via Defect Modulation for High-Performance Aqueous Zn-Ion Batteries

*Yi-Yen Hsieh, Yu-Chun Chuang, and Hsing-Yu Tuan**

Developing cathode materials for aqueous zinc-ion batteries (ZIBs) that offer high capacity, rapid charge–discharge rates, and prolonged cycle life remains a significant challenge. This study explores the use of zipper-type Bi_2O_2Se nanoplates modified by selenium vacancy (V_{se}) modulation, which reduces electron scattering, enhances carrier mobility in [Bi_2O_2] conducting channels, and decreases coulombic interactions within electrostatic layers. The introduction of Se vacancies facilitates electron transfer from the host to [Bi_2O_2] channels and reduces scattering in the [Bi_2O_2] framework, thus improving carrier mobility. These Se-poor Bi_2O_2Se nanoplates demonstrate a greater affinity for zinc ions, reduced diffusion barriers, and faster transport kinetics, which enable more efficient Zn-ion insertion, tripling the electrochemical capacity, improving rate capabilities, and extending cycling life. Enhancements such as reinforced structural integrity and expanded interlayer spaces support a dual Zn-ion-driven mechanism involving both insertion and conversion reactions, essential for superior electrochemical storage performance. The results include an impressive discharge/charge capacity of 380.3 mA h g^{-1} at 0.1 A g^{-1}, a cycle life of up to 10 000 cycles at 5 A g^{-1}, and a current tolerance exceeding 10 A g^{-1}. This research highlights how nano- and defect engineering of Bi_2O_2Se can significantly enhance ionic conductivity, expedite electron transfer, and improve Zn-ion diffusion.

1. Introduction

The rising global energy consumption, coupled with the depletion of natural resources and increasing environmental pollution, highlights the critical need for advanced energy storage technologies. Lithium-ion batteries (LIBs) currently lead in energy storage applications across electric vehicles, portable electronics, and grid storage due to their high energy density. However, concerns over the safety of the toxic and flammable organic solvents used in LIBs prompt a shift toward safer, water-based electrolyte solutions. Multivalent-ion aqueous batteries emerge as compelling alternatives, offering advantages such as a high theoretical capacity of 820 mA h g^{-1}, a favorable redox potential of 0.76 V versus the standard hydrogen electrode, cost-effectiveness, and enhanced safety.[1–3] This shift toward aqueous batteries, particularly zinc-ion batteries (ZIBs), signifies a crucial step in overcoming the safety and sustainability challenges linked to conventional LIBs.[4,5] Despite the multiple advantages, the wide-scale application of ZIBs is limited by either inferior cycling lifespan or weak tolerance for current abuse originating from unstable cathode materials and sluggish diffusion kinetics of divalent Zn ions in the host frameworks. Therefore, recent studies focus on how to optimize the aqueous ZIBs through electrolyte design strategies and metal anode modification.[6–11] Addressing these issues is crucial for unlocking the full potential of ZIB technology and facilitating its broader integration into energy storage applications.

Numerous studies are dedicated to the development and design of cathode materials, including layered cathodes, tunnel cathodes, and carbonaceous cathodes.[12] Particularly, the layered materials and tunnel materials are respectively composed of weak van der Waals (vdW) interaction and chemical bonding in three dimensions, encompassing metal oxides (e.g., vanadium- and manganese-based compounds[13,14]) and metal chalcogenides. Despite these efforts, many cathode materials struggle to meet desired performance benchmarks. The challenges in ZIB cathode materials largely arise from slow insertion/extraction kinetics due to narrow gaps and tunnels with strong electrostatic interactions, as well as electrode degradation from structural instability. To address these, researchers are deliciated to optimize cathode materials, decrease the electrostatic interaction, expand the interlayer space, and enhance the active sites through surfactant/polymer addition,[15,16] additional cation introduction,[17] oxygen vacancy modulation,[18] exfoliation and nanosized engineering,[19,20] etc. Optimal cathode material selection and strategic structural engineering are imperative

Y.-Y. Hsieh, H.-Y. Tuan
Department of Chemical Engineering
National Tsing Hua University
Hsinchu 30013, Taiwan
E-mail: hytuan@che.nthu.edu.tw
Y.-C. Chuang
National Synchrotron Radiation Research Center
Hsinchu 30076, Taiwan

The ORCID identification number(s) for the author(s) of this article can be found under https://doi.org/10.1002/adfm.202406975

DOI: 10.1002/adfm.202406975

for the development of high-performance aqueous ZIBs, aimed at maximizing zinc ion storage capacity while ensuring structural durability. Currently, the principal challenge impeding the widespread adoption of ZIBs in aqueous environments is the lack of cathode materials that meet all essential performance criteria. These criteria include: 1) a stable crystal structure for enduring cyclability, 2) adequate specific capacity to store energy efficiently, 3) a high discharge voltage plateau for optimal energy output, 4) tailored morphological designs that preferentially host Zn ions over protons, and 5) enhanced mechanisms to overcome the inherent slow kinetics and ion diffusion challenges associated with Zn ions.[7] Addressing these factors is crucial for unlocking the full potential of ZIB technology in advanced energy storage applications.

Quasi-2D [Bi_2O_2]-based layered materials have emerged as a promising cathode choice for aqueous ZIBs, driven by their atomic-thin structure and unique properties. These materials have attracted significant interest across various research areas, including as photocatalysts,[21,22] thermoelectric materials,[23] and energy storage materials.[24] Due to their combination of strong intralayer covalent bonds and weak interlayer interactions, this allows them to form few-layered 2D crystals.[25,26] Bi_2O_2Se, in particular, stands for its high carrier mobility, moderate band gaps, and superior electronic properties, positioning it as an ideal material for channel applications.[27–29] Structurally, Bi_2O_2Se is an ionic compound, featuring a structure where covalently bonded [Bi_2O_2] layers are interspersed with planar Se layers through weak electrostatic interactions. Recently, it has been shown that bulk Bi_2O_2Se synthesized via solid-state methods demonstrates strong interlayer interactions, which hinder the insertion of Zn ions, favoring only hydrogen ion insertion into its layers.[30,31] The insertion barrier for Zn ions in Bi_2O_2Se limits its electrochemical capacity, failing to meet essential performance criteria. Also, the by-products formed by electrolyte salts and OH anions will be facilitated due to the usage of proton charge carriers. The corresponded voltage plateau of proton insertion is located at a range of 1.2–0.8 V, while the participation of Zn ions is below 0.8 V.[32] Therefore, enabling Zn ions access in zipper-type materials like Bi_2O_2Se is crucial for overcoming its limitations in aqueous ZIBs.

This study demonstrates that Bi_2O_2Se nanoplates can effectively reduce the coulombic interaction between electrostatic layers, enabling Zn-ion insertion and tripling the electrochemical capacity. As shown in **Scheme 1**, the Bi_2O_2Se supports a quasi-layered [Bi_2O_2] framework that facilitates continuous Zn-ion insertion, mirroring the behavior of layered materials. Zn ions, once inside the layers, react with Se to form Zn-Se compounds, thereby enhancing the electrochemical capacity through increased mobility of charge carriers. Most importantly, the electrochemical performances of Bi_2O_2Se are influenced by Se-rich and Se-poor conditions, having an impact on carrier mobility and structural integrity. The presence of Se vacancies inhibits the interference from the electron donor sits to the [Bi_2O_2] conducting channels, while the [Bi_2O_2] layers without any replacement of Bi atoms reduce the electron scattering effect in [Bi_2O_2] framework, thereby enhancing carrier mobility of Bi_2O_2Se. In other words, the covalently bonded [Bi_2O_2] layers remain stable and are not compromised by excess Se, which will replace Bi atoms and disrupt the [Bi_2O_2] layers. The enhancement of electronic properties of Se-poor Bi_2O_2Se can strengthen the Zn-ion affinity and carrier mobility, while structural stability and integrity of [Bi_2O_2] layers can improve the reversibility of insertion and conversion reactions during the cycling process. By modifying the electrostatic layers of Bi_2O_2Se to increase Zn-ion affinity and reduce the diffusion barrier, charge transport resistance is lowered, and high-frequency redox reactions are enhanced under higher current densities. This demonstrates the potential of zipper-type Bi_2O_2Se in aqueous batteries and offers crucial insights for future battery design and development.

2. Results and Discussion

2.1. Material Characterization and Features for Zipper 2D Architecture, $[Bi2O2]^{2+}$ Layer, and Selenium Vacancies

2D Bi_2O_2Se nanomaterials were synthesized using the molten salt hydrothermal method, which controls their lateral dimensions by adsorbing cations such as Li and K onto the (001) plane. Growth along the [001] direction is limited, depending on the concentration and electronegativity of the cations.[33] Quasi-2D Bi_2O_2Se features a unique structure with covalently bonded $[Bi_2O_2]^{2+}$ oxide layers and electrostatic Se layers, differing from vdW layered materials.[29] It is an ionic layered material with alternating [Bi_2O_2] cation and [Se] anion layers along the *c*-axis, connected by weak electrostatic interactions. As shown in **Figure 1a**, the cross-sectional HRTEM image reveals Bi_2O_2Se nanoplates stacked in two layers, with lattice growth oriented along the [001] direction, as confirmed by the SAED pattern (Figure 1b). To observes the lateral structure of Bi_2O_2Se, STEM image shows the electrostatic layers and covalent bonded layer of Bi_2O_2Se based on different atomic number. The fitted d-spacing of interlayer is coincided with the (004) plane (see Figure 1c and inset). The molecular structures in Figure 1d clearly show the lateral composition of $[Bi_2O_2]^{2+}$ and Se layer with an [001] stacking direction. Due to the electronegativity and electron localization, the two O atoms near Bi atom causes an increased ionicity of the Bi-chalcogen bonds, illustrating that the Bi and O atoms will exhibit stronger chemical bonding than Bi and Se atoms.[34] Consequently, after forming $[Bi_2O_2]^{2+}$ layers, the Se atoms will break away from covalent Bi—Se bonds and connect with $[Bi_2O_2]^{2+}$ layers through electrostatic interactions. The zipper-like structure of Bi_2O_2Se significantly differs from traditional layered materials, which are stacked by vdW force without any dangling bonds between the layers. The mixed molten salt has a strong polarizing power to solvate the solid precursors, accelerate mass transfers, reduce the surface energy, and, as a result, facilitate the lateral assembly growth of thinner layered material in a fluid phase.[35] In the molten salt growth process, the anions and cations of salts strongly interact with the surfaces of inorganic lattices, altering the surface energy of specific planes. This alteration can accelerate or retard the growth of crystal facets, leading to specific morphologies. Moreover, the use of molten Li- and K-based salts is particularly valuable due to their peeling ability when heated. As a result, Bi_2O_2Se can achieve a relatively thin morphology and high aspect ratio, making it suitable for layered materials.[36] Simultaneously, adding PVP surfactant, with its long chains and electrophilic groups, improves growth orientation and shape control in Bi_2O_2Se synthesis, also preventing Bi_2O_3 impurities.[37]

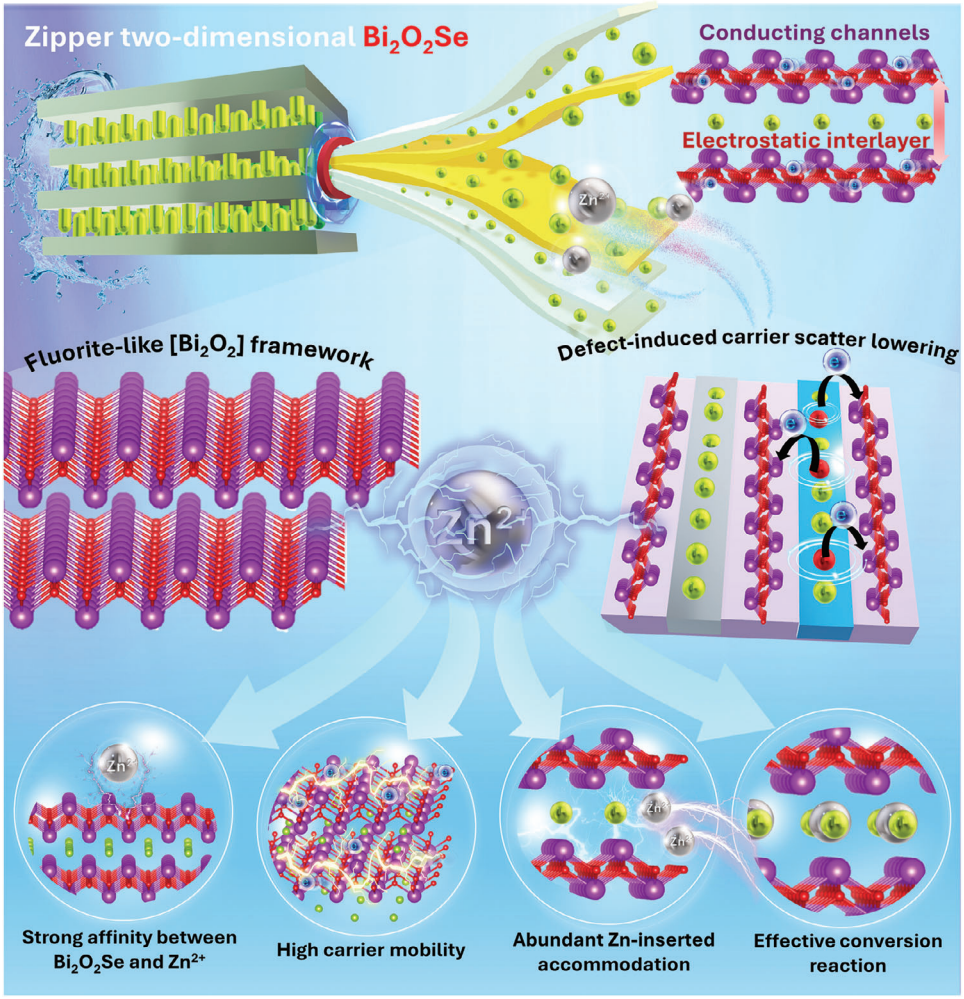

Scheme 1. Schematic illustration of unique zipper 2D Bi_2O_2Se and its advantages for Zn-ion insertion. The quasi-layered Bi_2O_2Se composed of fluorite-like $[Bi_2O_2]$ conducting channels and defect-induced carrier scatter lowering enhances the carrier mobility and Zn-ion affinity, further improving the fast transport kinetics and diffusion barrier on Bi_2O_2Se. The structural stability of $[Bi_2O_2]$ framework as a Zn-ion storage layer can facilitate the reversibility of redox reactions during the cycling process, simultaneously promoting conversion reaction between inserted Zn ions and Se atoms within electrostatic layers. The electrochemical capacity and cyclability of Bi_2O_2Se cathode can be greatly improved in aqueous ZIBs.

The carbonyl group of PVP will adsorb on the (001) plane, while the long-chain carbon can enhance the electrostatic interaction of $[Bi_2O_2]^{2+}$ layer, inhibiting the vertical growth and aggregation of Bi_2O_2Se nanoplates. Through the PVP and hybrid molten salt-assisted surface control, Bi_2O_2Se nanoplates are fabricated as its lateral size range from 300 to 700 nm. Furthermore, top viewed TEM image (Figure 1e) reveals a thin layer of Bi_2O_2Se with two lattice planes of (110) and (200)/(020) of Bi_2O_2Se, as confirmed by the HRTEM image and iFFT pattern in Figure 1f and Figure S1 (Supporting Information). The spot pattern from SAED (Figure 1g) provides evidence for the presence of (200), (002), and (110) lattice planes at zone axis of [001] direction. The top viewed STEM image of Bi_2O_2Se shows the lattice arrangement of Bi atoms on the (001) face (Figure 1h). As shown in Figure 1d, the relative position of Bi atoms and lattice growth directions in Bi_2O_2Se are consistent with results of electron microscopy. The elemental distribution and composition of Bi, Se, and O of Bi_2O_2Se are proved by EDS mapping (Figure S2, Supporting Information). In order to comparison of structural features, we fabricated various Bi-based materials, including vdW layered Bi_2O_5Se with tunnels, tunnel Bi_2O_3, and vdW layered Bi_2Se_3, using similar hydrothermal methods (Figure S3, Supporting Information). The XRD patterns (Figure S4, Supporting Information) confirm that Bi_2O_2Se, Bi_2O_5Se, Bi_2Se_3, and Bi_2O_3 are designated as tetragonal, orthorhombic, rhombohedral, and monoclinic crystal structures, respectively (Figure S5, Supporting Information). The corresponding SEM images of these materials are displayed in Figure S6 (Supporting Information). In addition, we synthesized the Bi_2O_2Se under Se-poorness and Se-richness conditions through the molar concentration of Se precursor. The Se content of Bi_2O_2Se can be adjusted by the addition of Se precursor, which is larger and smaller than 1 mmol due to the Bi/Se ratio of 2:1. The corresponding XRD pattern given in Figure S7 (Supporting Information) shows that the Se-rich Bi_2O_2Se has a thinner thickness than Se-poor Bi_2O_2Se based on Scherrer's formula. According to the SEM images of Bi_2O_2Se

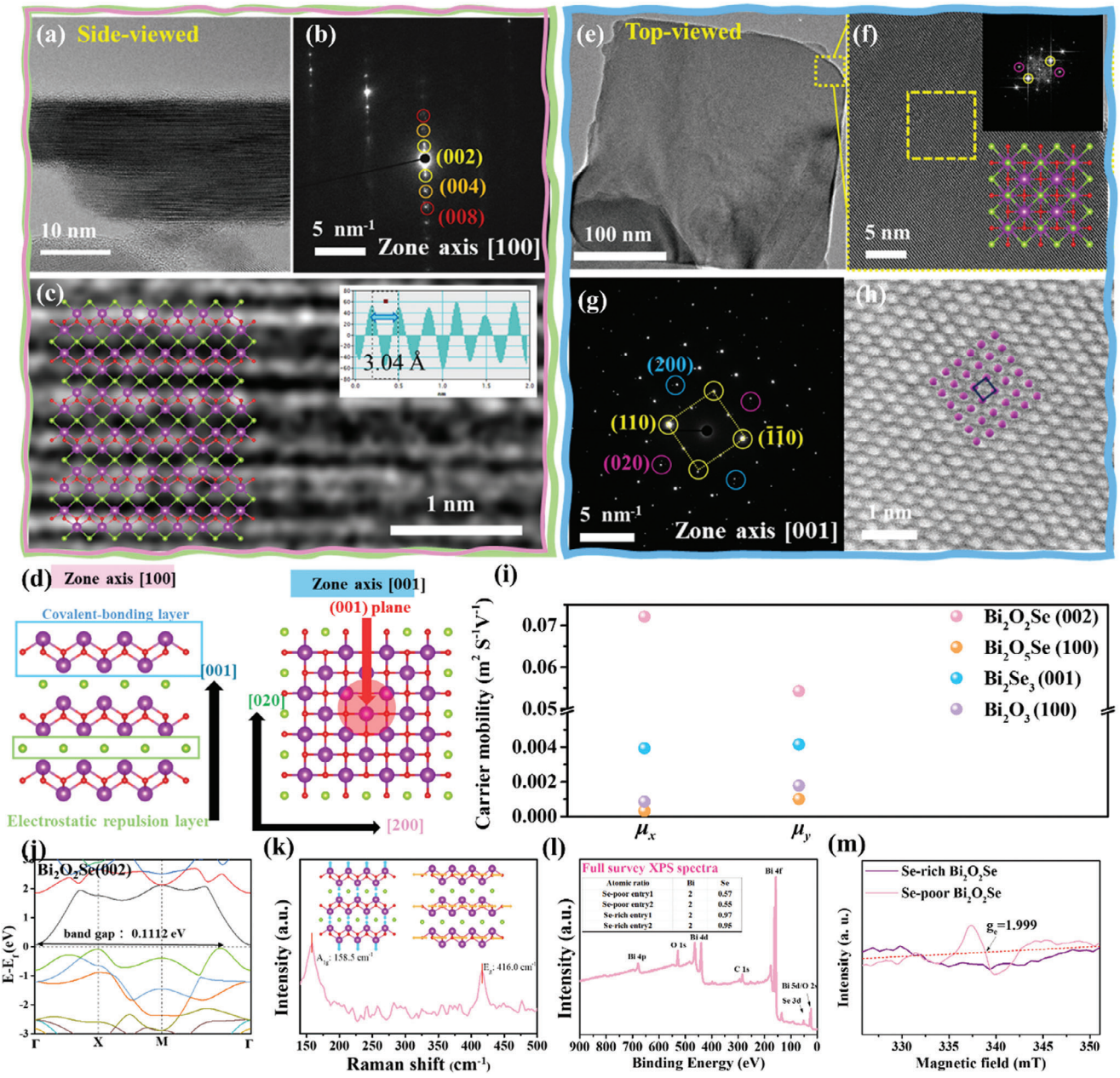

Figure 1. a–c) HRTEM image, SAED pattern, and HAADF-STEM image of side viewed Bi_2O_2Se at zone axis of [100]. d) Molecular structure of side viewed and top viewed Bi_2O_2Se. e–h) TEM image, HRTEM image, SAED pattern, and HAADF-STEM image of top viewed Bi_2O_2Se at zone axis of [001]. i) Simulated electron carrier mobility of Bi_2O_2Se (002), Bi_2O_5Se (100), Bi_2Se_3 (001), and Bi_2O_3 (100) along the *x*-axis and *y*-axis. j) The Band structure of Bi_2O_2Se (002). k) Raman spectra and vibration modes of Bi_2O_2Se. l) The full XPS survey spectra and Bi/Se ratio of Se-poor and Se-rich Bi_2O_2Se. m) EPR spectra of Se-poor and Se-rich Bi_2O_2Se.

under two conditions (Figure S8, Supporting Information), there is a clear difference between Se-poor and Se-rich Bi_2O_2Se, which are nanoplates and nanosheets, respectively. This may be attributed to the preferential Se-termination in the Se-rich condition, which is more significantly affected by hybrid salt cations than in the Se-poor condition.

The ultrahigh carrier mobility of bulk Bi_2O_2Se has been performed owing to its unique structure, in which the strong covalently bonded [Bi_2O_2] layers are sandwiched by planar [Se] layers with a relatively weak electrostatic interaction.[27,29] Consideration of structural features, bulk Bi_2O_2Se semiconductors possesses a moderate band gap and ultrahigh carrier mobility due to its weak bond strength with electrostatic interaction along the *c*-axis.[27] There is a relationship between band gap and carrier mobility in semiconductors; however, it can be varied with factors like crystal structure and defects. In general, a larger band gap typically leads to lower carrier mobility, while a smaller band gap can result in higher carrier mobility. This is because in

materials with a larger band gap, the energy required for electrons to move from the valence band to the conduction band is larger, resulting in lower carrier mobility. Conversely, the required transition energy in a smaller band gap of materials is lower, leading to higher carrier mobility. In our study, we selected specific lattice planes based on their stacking direction and layered nature, while non-layered Bi_2O_3 is chosen for its tunnel structure formed by Bi—O layers. These chosen crystal facets of all materials also consist in the TEM and XRD results. Therefore, we employed density functional theory (DFT) calculations to analyze the electronic properties of the semiconductors. As shown in Figure 1i and Table S1 (Supporting Information), the calculated carrier mobility of Bi_2O_2Se (002) is significantly higher than other layered and tunnel materials in an order of Bi_2O_2Se > Bi_2Se_3 > Bi_2O_3> Bi_2O_5Se. This is because the relationship between band gap and carrier mobility as given in Figure 1j and Figure S9 (Supporting Information). An indirect band gap of Bi_2O_2Se (002) is located at 0.1112 eV with a valence band maximum and conduction band minimum at respectively X and Γ point. Bi_2Se_3 follows a similar trend with a band gap of 0.8946 eV. Conversely, the Bi_2O_5Se has a larger band gap of 3.1121 eV with both VBM and CBM at the Γ point. The Bi_2O_3 also exhibits a wider band gap of 2.4903 eV, and both Bi_2O_5Se and Bi_2O_3 have a direct band gap. In addition, the carrier mobility of Bi_2O_2Se (001) cannot be calculated due to its conductor property, and, therefore, we choose (002) face of Bi_2O_2Se to compare with other materials in this work. Carrier mobility, proportional to conductivity ($\sigma = ne\mu$) at constant charge concentration (n), shows Bi_2O_2Se (002) has superior conductivity and mobility. This implies the $[Bi_2O_2]$ channels effectively facilitate the movement of charge carriers, including electrons and zinc ions, through the interlayer and surface of Bi_2O_2Se.

To analyze the unique Bi_2O_2Se architecture, Raman spectrum (see Figure 1k) exhibits two vibration mode of Bi—O assigned as out-of-plane (blue arrow, 158.5 cm^{-1}) and in-plane (orange arrow, 416.0 cm^{-1}) of $[Bi_2O_2]$ layers.[38,39] Raman of Bi_2O_3, Bi_2O_5Se, and Bi_2Se_3 are coincided with previous literatures (Figure S10, Supporting Information).[40–42] To confirm the presence of Se vacancies (V_{Se}), relative Bi/Se ratio is calculated from XPS results based on the relationship between peak area and relative sensitivity factors ($A = n \times RSF$). The atomic ratio of Bi to Se on the surface of Bi_2O_2Se nanoplates is obtained by XPS analysis under Se-poor and Se-rich conditions (Figure 1l; Table S2).[43,44] Under Se-poor conditions, Se ratios in Se-poor Bi_2O_2Se are ranged from 0.55 to 0.57 with a Bi ratio of 2. Conversely, under Se-rich conditions, the excessive molar concentration of Se precursor can ensure the Bi/Se molar ratio of 2:1, which is consistent with stoichiometric ratio of Bi_2O_2Se. This highlights the tunability of Se content in Bi_2O_2Se, confirming the presence of V_{Se} within the layers. Additionally, the splitting peaks of Bi 4f located at 162.4 and 157.1 eV belong to the 4f 5/2 and 4f 7/2 of Bi (III) in the Bi_2O_2Se lattice (Figure S11, Supporting Information). The two couples of splitting peaks of Se 3d are located at 52.3/53.2 and 56.7/57.9 eV, which are respectively attributed to the Se^{2-} in Bi_2O_2Se crystal and SeO_x formed on the crystal surface.[45] The O 1s XPS spectra are resolved to 529.7 and 530.2 eV belongs to the Bi—O bonds in the $[Bi_2O_2]^{2+}$ layer of Bi_2O_2Se crystal, while the XPS peak of adsorbed O on crystal surface is located at 533.6 eV.[21,46] The XPS analysis proves the high quality and purity of as-prepared Bi_2O_2Se powder. Besides, based on different chemical environment and atomic electronegativity, electron density of Bi (III) would be reduced with the upshift of XPS peaks as the number of high electronegative atoms increased. As shown in Figure S12 (Supporting Information), the sequence of Bi 4f peaks across the materials—Bi_2O_5Se < Bi_2O_3 < Bi_2O_2Se < Bi_2Se_3—matches the electronegativity sequence (O (3.44) > Se (2.55) > Bi (2.02)) and the Se/O atomic number. Apart from the oxidation on the surface of Bi_2Se_3, the other compounds display air stability, so only one couple of splitting peaks of Bi 4f can be seen. EPR spectra, as illustrated in Figure 1m, utilize the Zeeman effect to identify Se vacancy-induced lone pairs, with unpaired electron spin resonance evident at a g-factor of 1.999 in Se-poor Bi_2O_2Se.

2.2. Electrochemical Performance and Impacts of Structural Engineering and Interfacial Modulation

To demonstrate the significance of structural engineering and interfacial modulation, electrochemical performances and kinetics of ZIBs can be enhanced. The structural advantages of zippertype Bi_2O_2Se are displayed by CV curve at low and high scan rates (**Figure 2**a). Due to its quasi-layered structure and Se atoms in the interlayers, this supports capacity through both insertion and conversion reactions, outperforming other materials examined. The quasi-layered structure of Bi_2O_2Se enhances electrolyte penetration into electrostatic layers, increasing Se atom reactivity. The covalently bonded $[Bi_2O_2]$ layers preserve Zn-ion insertion capacity and enhance reversibility of conversion reaction during cycling. The highly electronegative Se layer and highly mobile electron carriers will facilitate the charge carriers from bulk electrolyte (i.e., Zn ions) and electric circuit (i.e., electrons) insert into the Bi_2O_2Se, further reacting with active Se atoms. Talking about usual 2D layered materials, there are vdW gap in Bi_2O_5Se and Bi_2Se_3, which are beneficial for Zn-ion insertion with a stable layer nature. Therefore, the Bi_2O_5Se and Bi_2Se_3 are composed of covalently bonded Bi—O/Se—O and Bi—Se, respectively. That is why layered structures are attractive cathode materials in aqueous systems. However, although vdW layered materials perform good durability for the high frequency of redox reactions, their capacities are contributed by insertion reaction only. In addition, non-layered 3D structures like Bi_2O_3 can be infiltrated by electrolyte passing through the surface and small tunnels consist of $[Bi_2O_2]$ covalent framework without large contact area and abundant active sites. The CV curve of Bi_2O_2Se exhibits a larger Faradaic current response at a voltage range from 0.8 to 0.7 V at a low sweep rate of 0.1 mV s^{-1} (see Figure 2b). This implies that the insertion number of Zn ions in Bi_2O_2Se is higher than in other cathode structures. Afterward, the two-step conversion reaction of the host cathode can further contribute an attractive capacity ranging from 0.7 to 0.2 V. The Bi_2O_2Se has a small reduction overpotential, meaning that Bi_2O_2Se needs the lowest energy to start the cathodic reaction each cycle (see Figure 2c). By increasing the scan rate to 1.0 mV s^{-1} (see Figure 2d), both cathodic and anodic peaks of Bi_2O_2Se maintain good reversibility and rate durability without phase transformation and severe voltage shift. The Bi_2Se_3 presents a phase transformation with low-rate capability during the discharge process. Meanwhile, the Bi_2O_5Se exhibits better durability at a high current rate, but its current response

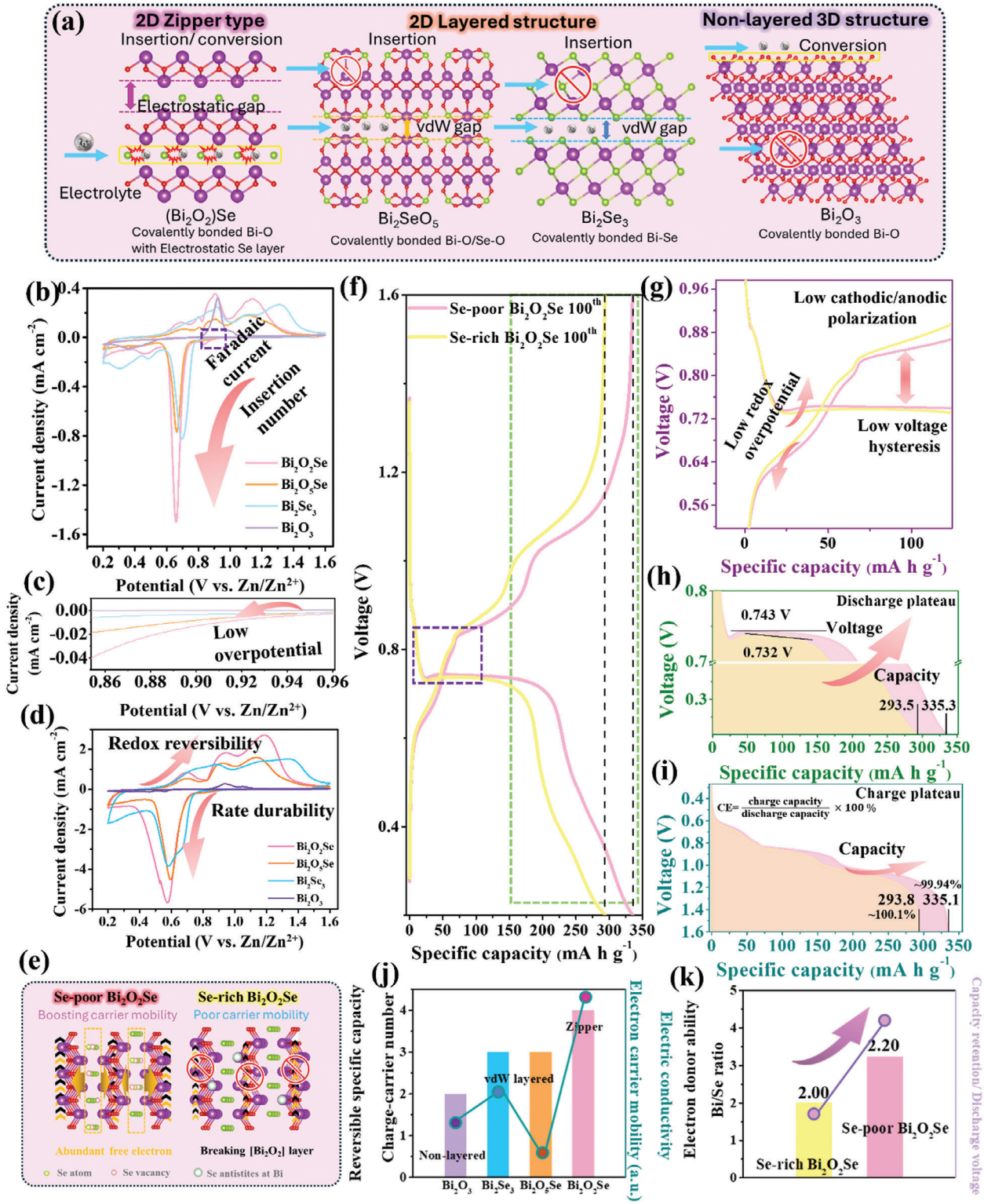

Figure 2. Electrochemical analysis of Se-poor Bi_2O_2Se in comparison of its structural uniquity and defect engineering. a) Structural illustration of Bi_2O_2Se, Bi_2O_5Se, Bi_2Se_3, and Bi_2O_3. b) CV curves of Bi_2O_2Se, Bi_2O_5Se, Bi_2Se_3, and Bi_2O_3 at first cycle at sweeping rate of 0.1 mV s^{-1}. c) Enlarged CV curves of Bi_2O_2Se, Bi_2O_5Se, Bi_2Se_3, and Bi_2O_3. d) CV curves of Bi_2O_2Se, Bi_2O_5Se, Bi_2Se_3, and Bi_2O_3 at sweeping rate of 1.0 mV s^{-1} after several cycles. e) Defect modulation with its advantages on structural scattering and carrier mobility. f) Voltage profiles of Se-poor and Se-rich Bi_2O_2Se after 100 cycles. The enlarged voltage profiles of Se-poor and Se-rich Bi_2O_2Se at different region: g) redox potential hysteresis, h) insertion and conversion plateaus at discharge process, and i) charge plateau and columbic efficiency. j) Structural and electrochemical advantages on Bi_2O_2Se compared with other materials. k) The capacity retention and discharge voltage of Se-poor Bi_2O_2Se and Se-rich Bi_2O_2Se.

is still worse than host materials. Furthermore, Bi_2O_3 displays a significant activation energy and inert electrochemical performances, leading to undesirable redox reversibility and current contributions during slow and fast cycling processes. The second highlight of this study is interfacial modulation, which can effectively open the advantages of the zipper-type Bi_2O_2Se structure. As shown in Figure 2e, the main conduction channel in Bi_2O_2Se is the $[Bi_2O_2]^{2+}$ layer that contributes to the ultrahigh carrier mobility. The $[Bi_2O_2]^{2+}$ as a conducting channel in Bi_2O_2Se lattice will be affected by the Se content.[47] Although the original $[Bi_2O_2]^{2+}$ layer can effectively transport the negative charge as a conducting channel, the electrons will center at the Se layers due to the high negative charge of Se atoms. Upon the formation of V_{Se} in the Bi_2O_2Se lattice, the electrons will transfer to the conducting $[Bi_2O_2]^{2+}$ channel, improving the carrier mobility and electron conductivity.[48] First, the lack of highly electronegative Se anion can relax the confined electrons around the electrostatic layers, leading to the abundance of free electrons flowing into the $[Bi_2O_2]$ channels and increasing the delocalized electrons. Besides, V_{Se} in the electrostatic layers will not affect the architecture of the main 2D conduction channels. Second, it may significantly destroy the main 2D conduction channels through Se antistites at Bi position under Se-rich conditions.[49] That is, the deficient Se content around electrostatic layers have a greatly impact on the $[Bi_2O_2]$ conducting channels and carrier mobility of Bi_2O_2Se. As given in the voltage profile of the 100th cycle at a current density of 100 mA h g^{-1} (see Figure 2f), we evaluated both Se-poor and Se-rich conditions consisting in Se content in the electrostatic layers of Bi_2O_2Se, which is respectively ≈10% deficient architecture and abundant Se content. The enlarged voltage curves in Figure 2g display that low voltage hysteresis and redox overpotential of Se-poor Bi_2O_2Se make its cathodic and anodic polarization decrease compared to Se-rich Bi_2O_2Se. This phenomenon can greatly improve cycling stability and reversibility at each cycle, leading to excellent retention and lifespan. Other merits benefited from the deficient Bi_2O_2Se structure are the higher voltage plateaus and larger reversible capacity magnified in Figure 2h,i. The discharge plateau of Se-poor Bi_2O_2Se (0.743 V) is higher than that of Se-rich Bi_2O_2Se (0.732 V). Although they have a slight difference in voltage height, they still exhibit a longer and higher voltage flat plateau under the same material system with a little bit of deficient modification. At the charge plateau of Se-poor Bi_2O_2Se, the charge capacity (335.1 mA h g^{-1}) is the same as the discharge capacity (335.3 mA h g^{-1}) with a decay percentage of 0.06%. Although the charge capacity of Se-rich Bi_2O_2Se is also close to its discharge capacity, its CE exceeds 100%, which can be ascribed to the irreversible shuttle effect of Zn-Se active materials during the charging process. Therefore, in response to the structural advantages (see Figure 2j), the boosted charge carriers and intrinsic carrier mobility of zipper Bi_2O_2Se can increase the reversible specific capacity and decrease the resistance with an enhanced electric conductivity. In other words, these electron carriers transported through fluorite-like $[Bi_2O_2]$ layers will facilitate the charge carriers (i.e., Zn ions) easily adsorb, diffuse, and insert into the $[Bi_2O_2]$-based interlayers. Furthermore, the electron donor ability of Se layers boosted by deficient sites can effectively stabilize the capacity retention and raise the voltage output (see Figure 2k). The greater the amount of Zn ion transfer, the higher the capacity. Most importantly, the intact Bi-O layer, free from any destructive substitution or decomposition, is the key feature that enables high-performance in aqueous batteries. Therefore, whether through structural engineering or interfacial modulation, there will be a positive impact on the electrochemical properties and performance.

The initial CV curves of the host cathode and other materials for the initial five cycles are displayed in **Figure 3**a and S13 (Supporting Information). Except for the initial irreversible reaction such as solid electrolyte interface (SEI) formation, all materials exhibit similar redox peak positions. However, Bi_2O_5Se and Bi_2O_3 can produce severe side reactions, leading to excessive electrolyte consumption and low CE. In addition to the rapid decay of the current response on the five initial CV curves, the other three materials all have activation behaviors under respective cycles of cathodic and anodic peaks. During the discharge process, the overpotential of the insertion and conversion reactions in Bi_2O_2Se showed a gradually decreasing trend from the first cycle to the fifth cycle (Figure 3b). The reduction in activation energy of reverse conversion and extraction of Zn ions will benefit the continuous process of redox reactions (Figure 3c). Notably, Se-rich Bi_2O_2Se provided better specific capacity in the first 25 cycles at a current density of 100 mA h g^{-1}, as given in Figure 3d. However, its capacity exhibits rapid decay, below 300 mA h g^{-1}, after 100 cycles. Surprisingly, Se-poor Bi_2O_2Se exhibits more stable cycling performance with attractive reversible capacity (>300 mA h g^{-1}), with a maximum capacity of 379 mA h g^{-1}. The capacity of layered Bi_2Se_3 was temporarily 302 mA h g^{-1} and then decayed to about 200 mA h g^{-1}, indicating that it could not sustain large Zn ion transmission numbers in repeated cycling tests. Layered Bi_2O_5Se with tunnels requires a longer period (about 50 cycles) for structural activation, but its capacity can still not meet the demand of up to 300 mA h g^{-1}. In addition, the Bi-based tunnel material Bi_2O_3 exhibits a highly irreversible phenomenon even during low current cycling. Figure 3e lists the corresponding voltage curves after the initial activation process. Compared with other materials, Bi_2O_2Se provides the longest discharge plateau, representing the insertion of a large number of zinc ions into the zipper layer, which is a key step for further conversion reactions with the Se layer. In addition, the capacity contribution ratio of the insertion and conversion reactions of Bi_2O_2Se is approximately 7:3. By the way, the phenomenon of IR drop in a material is crucial to ensure the current durability of the material when a current pulse is emitted from the resting state. Enlarged voltage curves in Figure 3f, there is the existence of IR drop in Bi_2O_3 and Bi_2Se_3 (black circle), which may be reflected in the rate capability. The rate performance of both Bi_2O_3 and Bi_2Se_3 (see Figure 3g) shows the fast capacity decay at current densities from 0.1 to 10 A g^{-1}. The Bi_2O_5Se has a stable stage at each current state; however, the capacity of Bi_2O_5Se decreases below 100 mA h g^{-1} under a current density of 3.5 A g^{-1}, which is similar to that of $Bi2Se_3$. The Se-poor Bi_2O_2Se performs the capacities of 369, 350, 317, 279, 244, 221, 198, 181, 167, 156, 146, 138, and 125 mA h g^{-1} at current densities of 0.1, 0.2, 0.5, 1, 1.5, 2, 2.5, 3, 3.5, 4, 4.5, 5, and 10 A g^{-1}, respectively, demonstrating the best rate capability and capacity performance even at 10 A g^{-1}. We also adopt the CV curves at various sweep rates from 0.1 to 1.0 mV s^{-1} to calculate the capacitive and diffusive contribution, which is respectively related to surface adsorption/desorption and Faradaic redox reaction (Figure S14, Supporting Information). Except for highly irreversible Bi_2O_3,

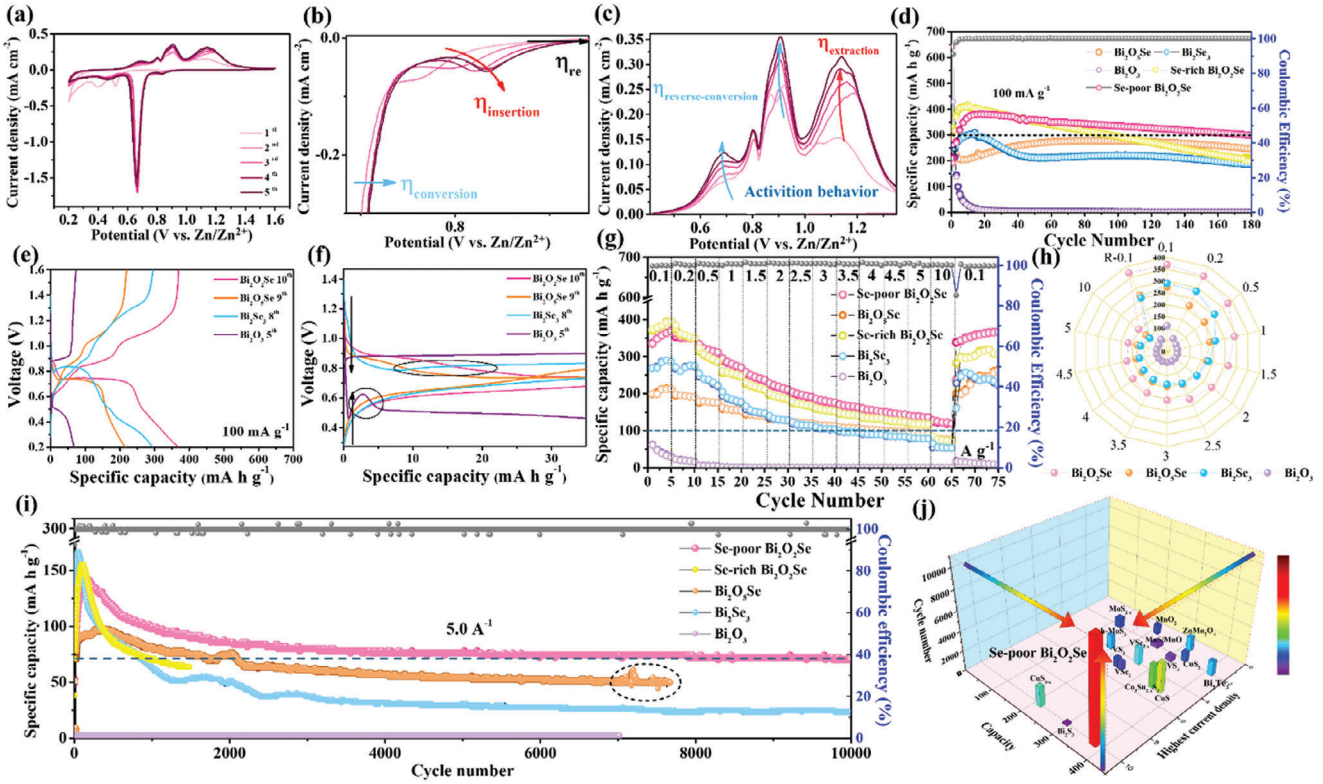

Figure 3. Electrochemical analysis and performances of Se-poor Bi_2O_2Se in aqueous ZIBs. a) CV curves of Se-poor Bi_2O_2Se for first five cycles. b) Enlarged CV curve of Se-poor Bi_2O_2Se at overpotentials of initial reduction, insertion, and conversion reactions. c) Enlarged CV curve of Se-poor Bi_2O_2Se at overpotentials of revere conversion and extraction reactions. d) Cycling performance at a current density of 100 mA h g^{-1}. e) Voltage profile of Bi_2O_2Se, Bi_2O_5Se, Bi_2Se_3, and Bi_2O_3 after activation at a current density of 100 mA h g^{-1}. f) Enlarged voltage profile at initial reduction and oxidation behavior of Bi_2O_2Se, Bi_2O_5Se, Bi_2Se_3, and Bi_2O_3. g,h) Rate performance and corresponding comparison of Bi_2O_2Se, Bi_2O_5Se, Bi_2Se_3, and Bi_2O_3. i) Cycling performance of Bi_2O_2Se, Bi_2O_5Se, Bi_2Se_3, and Bi_2O_3 at a current density of 5 A h g^{-1}. j) 3D comparison plot between Se-poor Bi_2O_2Se and other materials in previous literatures.[17,50–64]

the current response of CV curves of host and other materials is proportional to the sweep rates, whose contribution ratio can be calculated. As shown in Figure S15 (Supporting Information), Bi_2O_2Se provides a higher capacitive contribution at a fast sweep rate of 1.0 mV s^{-1}, indicating that its surface capacitive features can effectively buffer the slow ion response under high-current pulse and redox frequency. It is consistent with the good rate capability and cyclability at ultrahigh current density. The comparison radar plot in Figure 3h shows a clear relationship and large difference between the host cathode and other materials in this work. As shown in Figure 3i, long-term cycling performances at high current density can verify the electrochemical and structural stability of materials. The Se-poor Bi_2O_2Se performs outstanding cyclability with a capacity of ≈75 mA h g^{-1} after 10 000 cycles at a high current density of 5 A g^{-1}. The Se-rich Bi_2O_2Se and Bi_2Se_3 exhibit a higher capacity contribution for the initial state, but they cannot remain 50 mA h g^{-1} over 2000 cycles. The Bi_2O_5Se delivers a capacity of 50 after 6000 cycles, and its structure has been destroyed after 7000 cycles due to the drastic fluctuation of discharge and charge capacity, leading to CE instability (black circle). We list the cycle number, capacity, and highest current density reported in some literature related to metal oxides, metal chalcogenides, and layered materials in Figure 3j.[17,50–64] Se-poor Bi_2O_2Se exhibits excellent cycling performance, promising specific capacity, and excellent current durability, which is comparable to usual 2D vdW layered and 3D tunneling materials. To prove the structural integrity of Se-poor Bi_2O_2Se, the post-mortem SEM images and XRD patterns of Se-poor Bi_2O_2Se and Se-rich Bi_2O_2Se are given in Figures S17 and S18 (Supporting Information). The Se-rich Bi_2O_2Se was cracked into small flakes after the cycling process, which cannot retain its original morphology of nanosheets. Conversely, SEM images showed structural integrity and high reversibility of Se-poor Bi_2O_2Se nanoplates even after long cycles. Furthermore, the post-mortem XRD patterns also proved that the (004) plane of Se-poor Bi_2O_2Se still exists after long-term cycling. Meanwhile, the signal of Se-rich Bi_2O_2Se is dismissed and decomposed into Bi-O compounds, which influence the cyclability, rate capability, and capacity retention.

2.3. Simulation and Characterization of Zn-Ion Insertion and Conversion Mechanism

Operando and ex situ techniques were used to prove the dual mechanism of zipper-type Bi_2O_2Se in aqueous ZIBs. The Bi_2Se_3 and Bi_2O_3 are the materials of insertion-type mechanism in Zn-ion batteries proved by previous literature.[17,31] Besides, the

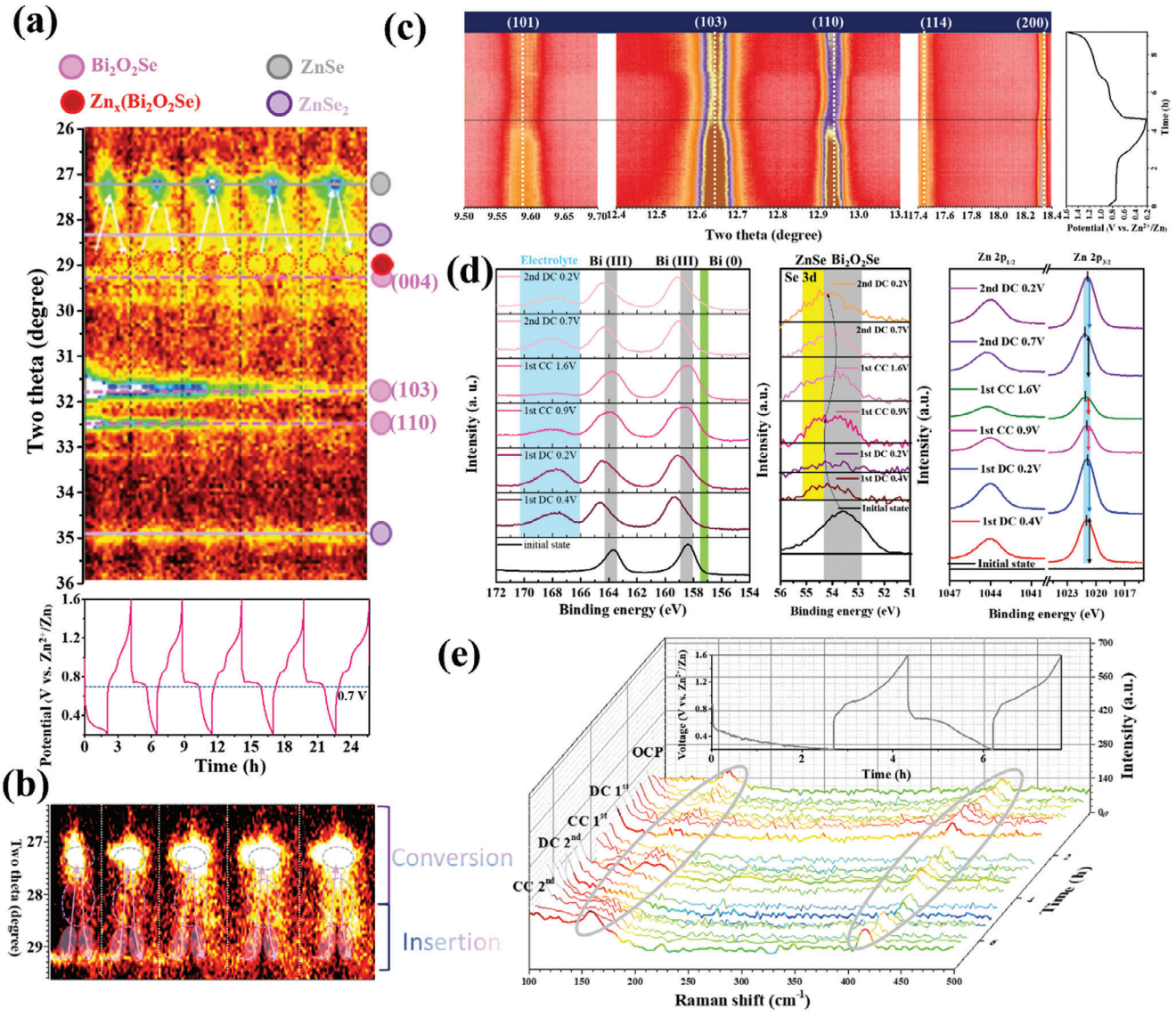

Figure 4. Analysis of Zn-ion storage mechanism in Bi_2O_2Se in aqueous ZIBs. a) The contour plot of the operando XRD pattern with magnified display ranged from 26° to 36°. b) The magnified display of the partial interval in the range of 27.3°–29.6° during insertion and conversion states for first five cycles. c) SXRD contour plot at specific lattice planes of Bi_2O_2Se. d) XPS spectra of Bi 4f, Se 3d, and Zn 2p after discharging to 0.2 V and charging to 1.6 V at the first and second cycle. e) 3D waterfall plot of Operando Raman spectra of Bi_2O_2Se for the first two cycles.

Bi_2O_5Se is also a novel cathode material in ZIBs, so its electrochemical mechanism is not available. The in-house Operando XRD contour plot is stacked alongside the voltage profile, illustrating the electrochemical evolution of Bi_2O_2Se over the first five cycles at various voltage stages (**Figure** 4a). The diffraction XRD signals located at 29.3°, 31.9°, and 32.6° belong to (004), (103), and (110) faces of Bi_2O_2Se (PDF 04-008-3129). When Zn ions are initially inserted into the electrostatic layer between $[Bi_2O_2]$ layers, the voltage drops to 0.4 V due to the higher energy to unlock the zipper's layer, which can be further proved by the voltage profile of coin cells at the first cycle in Figure S19 (Supporting Information). Moreover, the insertion overpotentials of Bi_2O_2Se significantly decreased at sequential cycles after loosening the strong electrostatic layers. The $Zn_x(Bi_2O_2Se)$ will convert to $ZnSe_2$ (28.3/34.9°, PDF 04-004-0999) and further transform into ZnSe (27.2°, PDF 00-037-1463) with the existence of $[Bi_2O_2]$ layers, which cannot further transform into metallic Bi and Zn-O compounds. The continuous existence of (103) and (110) faces of Bi_2O_2Se can prove this result. During the charging process, the conversion products are gradually reversely converted to (004) faces of Bi_2O_2Se. It is worth noting that only the (004) plane would be greatly affected during the cycling process, while both the (103) and (110) planes remained with a slight shift toward smaller two theta. As shown in the enlarged contour plot (Figure 4b), the Bi_2O_2Se (004) peak is shifted toward ≈28.5°, implying that the insertion of Zn ions expands the stacking interlayer along the *c*-axis. To confirm the shift of Bi_2O_2Se peaks along the *a*-axis and *b*-axis, the Operando synchrotron XRD is

used to analyze the slight signal shift at extremely fast data collection time (30 sec seq.$^{-1}$ num) without displacement. Figure 4c demonstrates a slight decrease in the intensity of each lattice plane during discharge, with the (110) and (200) planes notably shifting toward lower angles, indicating an expansion along the *a*- and *b*-axis due to continuous Zn ion insertion. Furthermore, ex situ XPS spectrum (see Figure 4d) of Bi_2O_2Se has been presented from the initial state to 2nd discharge state. The XPS analysis of Bi 4f shows the repetitive existence of the oxidation state of Bi, demonstrating the absence of Bi metal decomposed from $[Bi_2O_2]$ layers. The XPS upshifts toward higher binding energy at discharge voltage and downshifts back to the original position of binding energy. This may be attributed to the influence of electron density and bond strength change in the $[Bi_2O_2]$ layer during the Zn-ion insertion and conversion reactions. Besides, the binding energy of XPS signal at 166–170 eV is attributed to the TFSI-based electrolyte.[65] The upshift binding energy of Se 3d from 53.6 to 55 eV is due to the formation of Zn-Se compounds.[66] In Zn 2p spectra, the intensity and area of XPS peaks represent the content of Zn in Bi_2O_2Se cathode.[67] Except for the initial state, the XPS peaks of Zn 2p displayed a gradual increase and decrease respectively in the discharge state and charge state, which are correlated with Zn-ion insertion and extraction. The O 1s spectra are significantly affected by signals of air and electrolyte, which cannot specifically prove the existence of $[Bi_2O_2$ layer (Figure S20, Supporting Information). Therefore, the Operando Raman technique is used to perform the existence of $[Bi_2O_2$ layers. As shown in Figure 4e, the vibration modes of ≈159 and 416 cm^{-1} at the OCP state of the Operando holder are consistent with the raw material of Bi_2O_2Se powder, meaning that the holder will not affect the Raman signals of materials and no additional peak appears. The in-plane vibration mode (416 cm^{-1}) has a slight shift during the cycling process, but the in-plane Raman peak of the $[Bi_2O_2]$ layer did not exhibit a significant change. However, the weakening and broadening of out-of-plane mode is attributable to lattice relaxation and expansion and during the conversion reaction of Se layers with inserted Zn ions.[68,69] After extracting Zn ions from Bi_2O_2Se, both vibration modes of $[Bi_2O_2]$ layers shift back to the original position, indicating structural reversibility and stability.

To understand the Zn-ion insertion and conversion reaction, we use first-principles calculation to determine the limit on the number of carriers within a Bi_2O_2Se supercell. The molecular structures and corresponding formation energies of Zn insertion are listed in **Figure** 5a,b-upper, and Table S3 (Supporting Information). First, three Zn-inserted sites, which are Zn1, Zn2, and Zn3, are located respectively at the center of four Se atoms, between two Se atoms, and inside the $[Bi_2O_2]$ layer. The Zn1 exhibits the highest formation energy of insertion per unit (eV/atom), while the Zn3 displays severe lattice distortion even though it has the lowest energy density. Therefore, we choose Zn2 as our initial insertion structure to further insert Zn at the next stage. At the second Zn-inserted stage, symmetrical insertion sites are chosen to insert another Zn. The formation energies of insertion structures exhibit a slight difference between Zn2-Zn1 and Zn2-Zn2. Due to lower formation energy without lattice distortion, Zn2-Zn2 is assigned as the stable step and used to insert the third Zn. When inserting a third Zn ion inside Se layers, both Zn2-Zn2-Zn1 and Zn2-Zn2-Zn2 present supercell distortion. Thereof, the Zn2-Zn2-Zn2 maintains the fluorite-like $[Bi_2O_2]$ layer with a slight distortion of supercell compared with Zn2-Zn2-Zn1. In addition, the formation energy of Zn2-Zn2-Zn2 is lower than that of Zn2-Zn2-Zn1, leading to the facile trend of inserting a third Zn. Importantly, after inserting the fourth Zn ion, the Zn2-Zn2-Zn2-Zn1 shows the interlayer mixing of Zn ions in Se layers, demonstrating that there is potential for the formation of Zn-Se compounds. This simulation phenomenon coincides with the results of Operando analysis. Although the supercell distortion of Zn2-Zn2-Zn2-Zn1 is relatively more serious than others owing to more Zn ions inserted into the Bi_2O_2Se, it exhibits a much lower formation energy of Zn insertion. Meanwhile, these results of compound formation indicate that four Zn ions may be the limitation of Zn accommodation in Bi_2O_2Se, which is close to the specific capacity of Bi_2O_2Se with an insertion and conversion contribution ratio of ≈3:1 in the ZIB system. To clearly show the insertion energy of each stage, we further calculated the difference between (n-1) and (n) step, as given in Figure 5b-lower and Table S4 (Supporting Information). Before the interlayer chaos happens, the insertion energy at each stage is more and more low, meaning that there is a large driving force to induce the Zn-ion insertion between two $[Bi_2O_2]$ layers. Furthermore, the axis expansion and volume variation of Bi_2O_2Se are given in Figure 5c and Table S5 (Supporting Information). The *c*-axis of the Bi_2O_2Se supercell would expand with the increased Zn-insertion number, which is consistent with the downshift of the Operando XRD pattern. To compare with these supercells of insertion structures, the original Bi_2O_2Se cell has expanded toward a 2 × 2 supercell to observe the volume variation. The volume expansion is mainly dependent on the elongation of the c-axis due to the layered nature of zipper-type Bi_2O_2Se. Therefore, cell volume is directly proportional to the c-axis variation with increasing Zn-insertion number. Besides, the b-axis is proportional to the volume variation due to slight distortion before inserting the fourth Zn ion inside the $[Bi_2O_2]$ layer. The a-axis and b-axis show a random expansion and compression due to the obvious lattice distortion predicted by the simulation. This non-proportional expansion along the a- and b-axis can be confirmed by the synchrotron Operando XRD data. Moreover, the steep slope of the c-axis and volume variation present the limitation of Zn-ion insertion without crystal structure change as the third Zn is inserted into the Bi_2O_2Se interlayer. The slow slopes occur during the insertion stages of the first two and the final Zn ions. The initial slow slope indicates a stable insertion structure, suggesting that the interlayer can accommodate more than two Zn ions. The second slow slope reveals that quasi-steady-state Bi_2O_2Se, with its larger lattice distortion and interlayer chaos after inserting the fourth Zn ion, may facilitate the progress of the conversion reaction.

To visualize the structure and phase variation of Bi_2O_2Se, the ex situ TEM analysis is displayed at different discharge/charge voltages. The interlayer expansion of Bi_2O_2Se is shown in **Figure** 6a at DC 0.4 V at the initial cycle. The STEM images of side viewed Bi_2O_2Se and the corresponding intensity profile from blue line is displayed in the inset of Figure 6a. The d-spacing of the (004) plane is located at about 3.06 Å, showing that there is a higher barrier and small lattice expansion for initial Zn-ion insertion into electrostatic interlayers of Bi_2O_2Se. After initially discharging to 0.2 V (see Figure 6b), the conversion product of

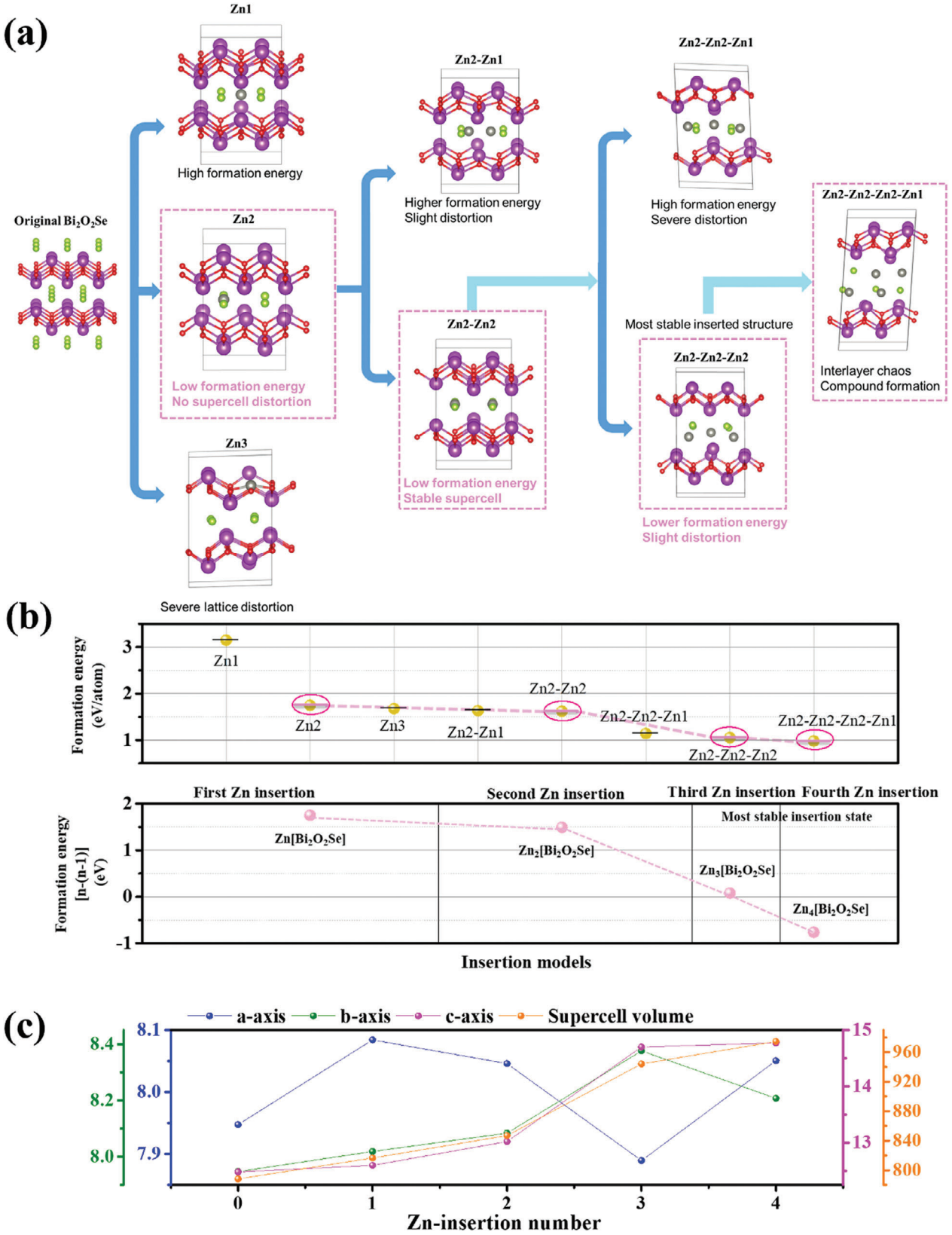

Figure 5. Theoretical simulation of storage mechanism of Bi_2O_2Se in ZIBs. a) The simulated molecular structures and different Zn-ion-inserted sites during the gradually inserting Zn ions. The supercells of Bi_2O_2Se with pink frame represents the preference of insertion sites. b) The formation energy at each insertion state. c) The variation of *a*-axis, *b*-axis, *c*-axis, and supercell volume during the stepwise Zn-ion insertion.

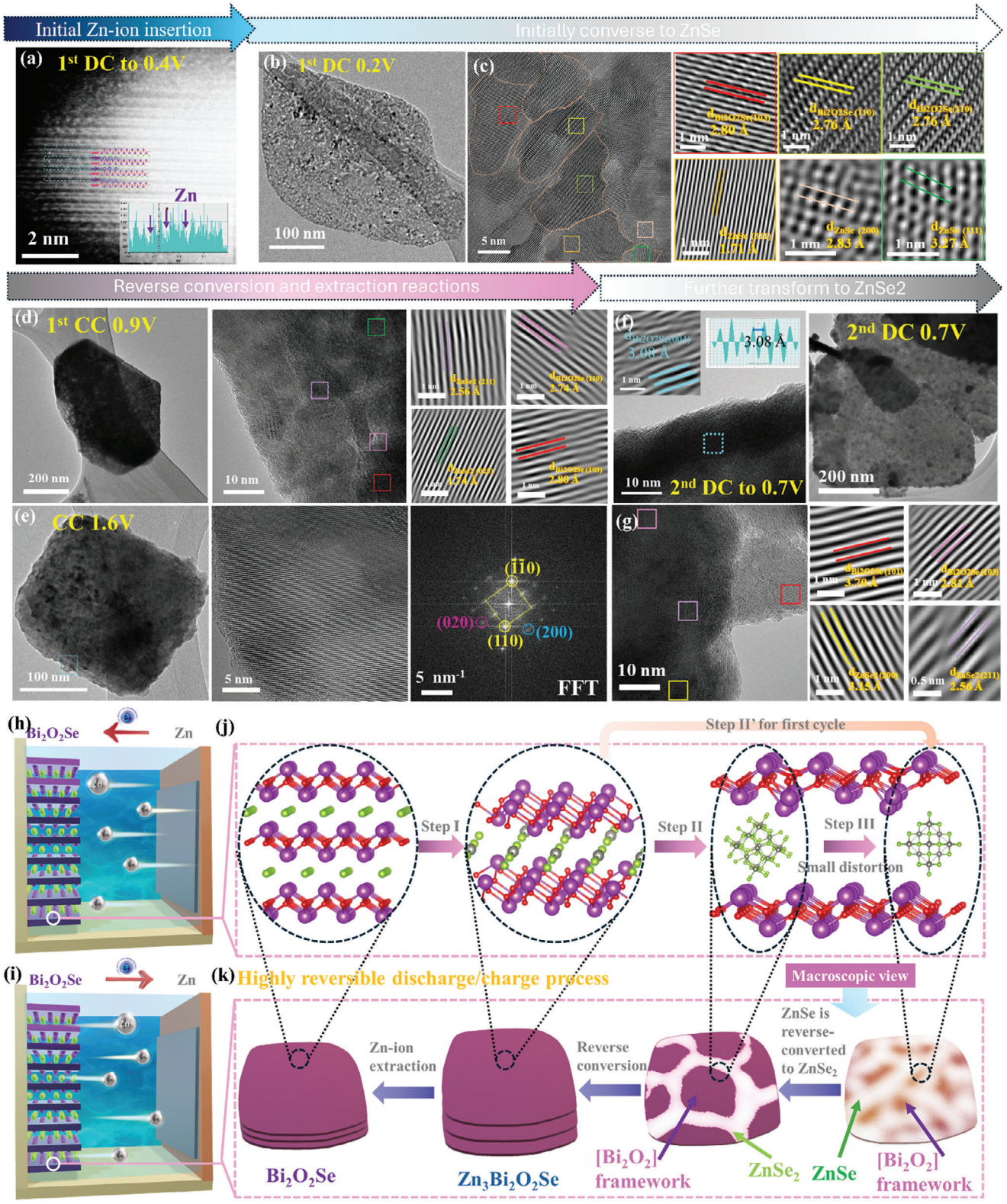

Figure 6. Post-mortem morphology and HRTEM images with corresponding FFT patterns of cycled Bi_2O_2Se: a) discharged to 0.4 V at first cycle, b,c) discharged to 0.2 V, d) charged to 0.9 V at first cycle, e) charged to 1.6 V at first cycle, and f,g) discharged to 0.7 V at second cycle. Schematic illustration of the Zn-ion storage mechanism with microscopic and macroscopic view during h, j) discharge and i, k) charging process.

the ZnSe phase forms instead of the conversion intermediate (i.e., $ZnSe_2$). The presence of many grains in the HRTEM image is linked to the low crystallinity in Operando XRD and Raman patterns. The d-spacing of (311), (200), and (111) faces of ZnSe are 1.71, 2.83, and 3.27 Å, respectively. The lattice variation of Bi_2O_2Se also exists in the iFFT patterns. Both (103) and (110) planes of Bi_2O_2Se are consistent with the trend of the SXRD contour plot. That is, the (110) plane expands to 2.76 Å, while the (103) plane remains at the original d spacing. The STEM image in Figure S21 (Supporting Information) also can prove the coexistence of ZnSe (400) and Bi_2O_2Se (110)/(200) at neighboring sites. During the charge process (see Figure 6d), HRTEM image at 0.9 V presents (211) and (023) planes of $ZnSe_2$, as well as (110) and (103) planes of Bi_2O_2Se. After completely charging to 1.6 V, an entire grain shown in the HRTEM image and FFT pattern in Figure 6e displayed the (001) exposed face with the projection of (110), (020), and (200) lattice points. To further show the difference between the first and second cycle, the HRTEM images (refer to Figure 6f) show a d-spacing of 3.08 Å corresponding to Bi_2O_2Se (004) face, indicating the expansion of the *c*-axis at 0.7 V of 2nd discharging process. It is worth noting that the expansion degree of the d-spacing of the (004) plane is close to the downshift of the diffraction peak in the XRD contour plot. As shown in Figure 6g, the appearance of Bi_2O_2Se and $ZnSe_2$ proves the structural stability of fluorite-like quasi-layers during the conversion process. In addition, $ZnSe_2$ will form at 0.7 V, which is located at the edge of the insertion plateau. Furthermore, the relationship scheme of the discharge and charge process of Bi_2O_2Se in ZIB system is displayed in Figure 6h,i. The electrochemical mechanism of molecular structure is shown in Figure 6j as below.

Thereof, "$Bi_2O_2Se_{1-2x}$" and "$Bi_2O_2Se_{1-y}$" represent the absence of Se in the Bi_2O_2Se lattice, assuming that the Se is incompletely converse to the Zn-Se compound. This depends on the difference between specific capacity (≈370 mA h g^{-1}) and theoretical capacity (≈406 mA h g^{-1}). Therefore, some Se atoms will exist in the $[Bi_2O_2]$ layers to maintain its crystal structure. The EDS mapping (see Figure S22, Supporting Information) demonstrates the uneven and uniform distribution respectively at full discharge and charge state, which is attributed to the formation of Zn-Se compounds and good reversibility of Bi_2O_2Se. Besides, the existence of Zn ions may be ascribed to the electrolyte remaining outside the Bi_2O_2Se surface. From the macroscopic view scheme in Figure 6k, the ZnSe and $ZnSe_2$ compounds would release and distribute near the Bi_2O_2Se grains during the discharging process. Although Bi_2O_2Se will not reverse to the smooth surface of nanoplates at a fully charging state, the small Bi_2O_2Se flakes can facilitate the sequential redox reaction, meaning that Zn ions can more easily insert into the interlayer of Bi_2O_2Se.

1st discharge process

$$\text{Step I: } Bi_2O_2Se + 3Zn^{2+} + 6e^- \rightarrow Zn_3\left(Bi_2O_2Se\right) \quad (1)$$

$$\text{Step III: } Zn_3\left(Bi_2O_2Se\right) + Zn^{2+} + 2e^- \rightarrow y\,ZnSe + Zn_{4-y}\left(Bi_2O_2Se_{1-y}\right)\ \left(y \leq 1.0\right) \quad (2)$$

1st charge process

$$\text{Step III: } y\,ZnSe + Zn_{4-y}\left(Bi_2O_2Se_{1-y}\right)\ \left(y \leq 1.0\right) \rightarrow x\,ZnSe_2 + Zn_{4-x}\left(Bi_2O_2Se_{1-2x}\right)\ \left(x \leq 0.5\right) \quad (3)$$

$$\text{Step II: } x\,ZnSe_2 + Zn_{4-x}\left(Bi_2O_2Se_{1-2x}\right)\ (x \leq 0.5) - Zn^{2+} - 2x\,e^- \rightarrow Zn_3\left(Bi_2O_2Se\right) \quad (4)$$

$$\text{Step I: } Zn_3\left(Bi_2O_2Se\right) - 3Zn^{2+} - 6e^- \rightarrow Bi_2O_2Se \quad (5)$$

2nd discharge process

$$\text{Step I: } Bi_2O_2Se + 3Zn^{2+} + 6e^- \rightarrow Zn_3\left(Bi_2O_2Se\right) \quad (6)$$

$$\text{Step II\&III: } Zn_3\left(Bi_2O_2Se\right) + Zn^{2+} + 2\,e^- \rightarrow x\,ZnSe_2 + Zn_{4-x}\left(Bi_2O_2Se_{1-2x}\right)(x \leq 0.5) \rightarrow y\,ZnSe + Zn_{4-y}\left(Bi_2O_2Se_{1-y}\right)\ (y \leq 1.0) \quad (7)$$

2.4. Electrochemical Kinetics and Diffusion Analysis

Ex situ EIS and GITT effectively demonstrate the impact of zipper-type Bi_2O_2Se's structural stability and electron carrier mobility on electrochemical kinetics. **Figure 7a** shows that, except for Bi_2Se_3, the other three materials exhibit similar charge-transfer resistance (R_{ct}) at OCP. By analyzing the diffusion-controlled region of EIS, we determine the Warburg factors, with the host materials exhibiting the lowest among the studied materials. This finding underscores the role of high-carrier-mobility $[Bi_2O_2]$ layers and highly electronegative Se layers in facilitating the passage of electrons and Zn ions, enhancing pre-reaction surface transport (Figure 7b). Besides, surface heterogeneities and geometry will induce non-uniform current and potential distribution, leading to a non-ideal semicircle.[70,71] After 180 cycles at 100 mA h g^{-1} (see Figure 7c,d), the zipper-type Bi_2O_2Se performs a lower R_{ct} and R_s compared to other structures, indicating that it contributes an electrochemical stability and ionic conductivity. Therefore, the layered Bi_2O_5Se presents the highest diffusion impedance, thereby leading to a long irreversible discharge plateau at the initial cycle. Meanwhile, high R_{ct} means a poor capability of charge carrier exchange and ion delivery inside a material, resulting in a lower capacity, large voltage hysteresis, and severe IR drop at each cycle. The non-layered Bi_2O_3 shows higher R_{ct} and Warburg impedance, which is consistent with its electrochemical performances and structural inactivity at OCP and 180th states. Except for the high R_{ct} and Warburg factor at the initial state, the vdW-layered Bi_2Se_3 displays a better capability for ion transfer and diffusion than Bi_2O_5Se and Bi_2O_3. Also, the structural cracking and passivation of cathode materials would cause an increased barrier for charge-carrier transfer

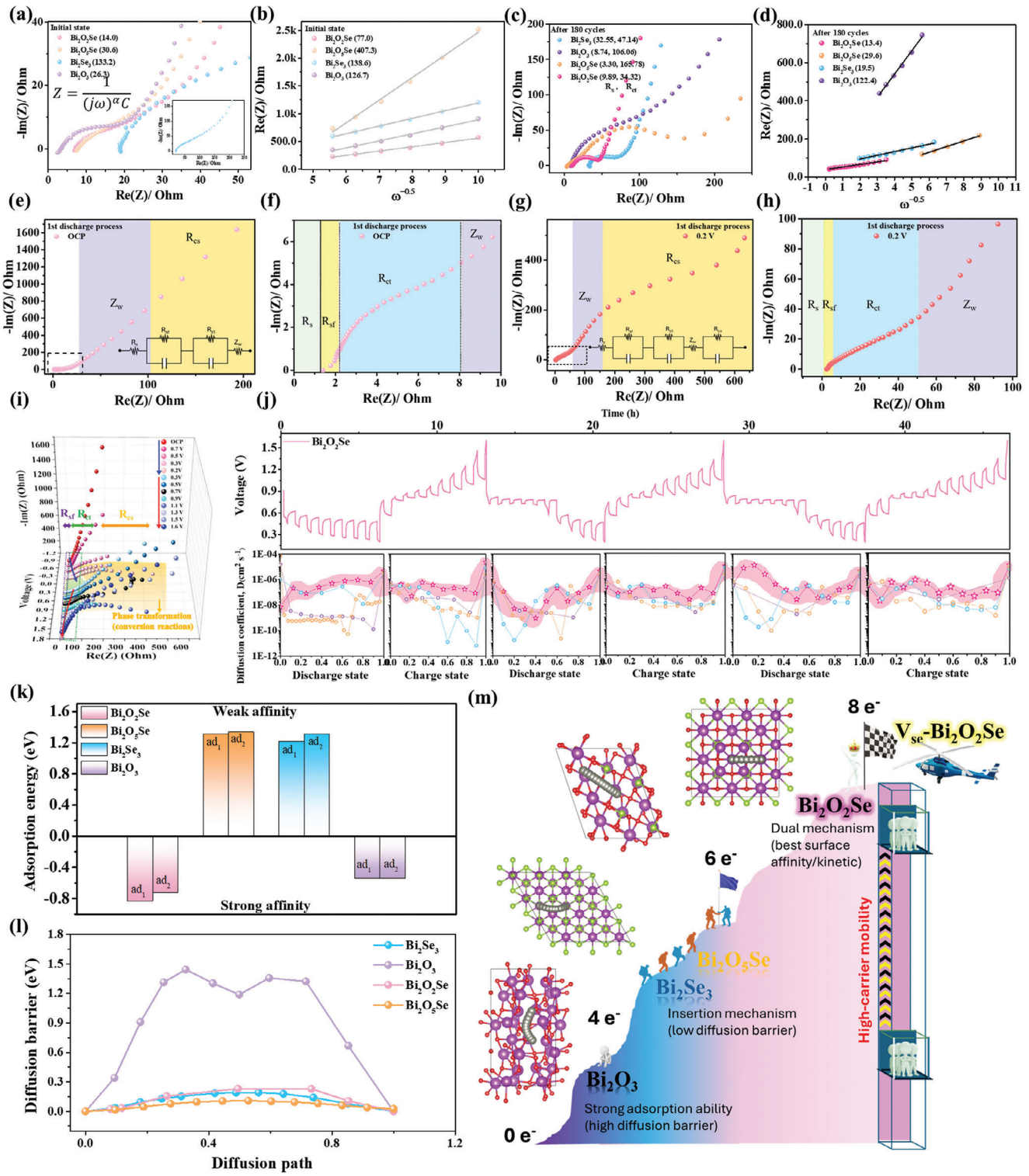

Figure 7. Kinetics analyses of the Zn-ion storage behaviors for Bi_2O_2Se cathode. Ex situ EIS spectra and linear diagram of impedance and frequency components of Bi_2O_2Se, Bi_2O_5Se, Bi_2Se_3, and Bi_2O_3 a, b) before and c, d) after 100 cycles. Nyquist plots and enlarged plot of Bi_2O_2Se at e, f) OCP and g, h) 0.2 V. i) In situ EIS spectra of Bi_2O_2Se during the initial cycling process. j) GITT curves with 10 mins current pulse of 100 mA g^{-1} followed by 30 mins relaxation and corresponding diffusion coefficients of each current pulse. k) Comparison of adsorption ability of Bi_2O_2Se, Bi_2O_5Se, Bi_2Se_3, and Bi_2O_3 for Zn ions. l) Energy barrier of Zn ion diffusion of Bi_2O_2Se, Bi_2O_5Se, Bi_2Se_3, and Bi_2O_3. g) The diffusion path in l) and comparison in Bi_2O_2Se, Bi_2O_5Se, Bi_2Se_3, and Bi_2O_3.

and solvated Zn-ion diffusion during continuous redox reactions. Herein, the Bi_2O_2Se exhibits the lowest kinetic barrier for ion adsorption and desorption and small overall resistance due to excellent carrier mobility and robust fluorite-like layers. Interestingly, the frequency range of in-situ EIS can investigate not only the resistance variation but also phase transformation.[72] As shown in Figure 7e,g, there are different equivalent circuits for OCP and discharge process of 0.2 V at a frequency range of 500 kHz–1mHz. With the decreasing of frequency, there is no semicircle appeared after diffusion control impedance at the OCP state. The enlarged region (Figure 7f) displays four zones for R_s, R_{sf}, R_{ct}, and Z_w. Thereof, the small R_{sf} may be ascribed to the PVDF binder distributed around the materials, which would not discuss in this work. As discharged at 0.2 V, the appearance of R_{cs} is induced by the change of the crystalline structure at extremely low AC frequency, further proving the ZnSe compound formation. The R_{ct} at 0.2 V is larger than that at OCP ascertained by the formation of ZnSe, as shown in magnified Nyquist plot of Figure 7h. Furthermore, in-situ EIS of Bi_2O_2Se, Bi_2Se_3, Bi_2O_5Se, and Bi_2O_3 are shown in Figure 7i and Figures S23-S27 (Supporting Information) for first cycle at a voltage range of 0.2–1.6 V. When the discharge voltage is lower than 0.5 V, the presence of R_{cs} confirms that the Zn ions insertion and conversion reactions occur with the continuous increase of R_{ct}. During the extraction of Zn ions, both R_{ct} and R_{cs} are repaired to the initial state, suggesting that the Bi_2O_2Se owns an excellent structural reversibility, which is similar to the resistance variation of the second cycle (Figure S23, Supporting Information). Importantly, the R_{ct} of Bi_2O_2Se maintains a smaller value (<50 Ohm) compared to other materials during the discharge and charge process. To further analyze diffusion behavior during the redox reactions, the GITT has been adopted to observe the variation of diffusion coefficients in ZIBs (Figure 7j; Figure S28, Supporting Information). The stable and fast diffusion coefficients demonstrate that Bi_2O_2Se performs excellent structural durability under the insertion of Zn ions during the redox reactions. On the condition of insertion and extraction states, both layered materials of Bi_2O_5Se and Bi_2Se_3 present sluggish Zn-ion diffusion around the surface and inside the interlayer. The Bi_2O_3 cannot deliver a stepwise GITT stage due to its high irreversibility after the first cycle.

To analyze the kinetic behaviors of these materials, DFT calculations were performed, focusing on the surface diffusion barrier and Zn-ion affinity before insertion reaction. The adsorption energy, indicative of the affinity between Zn ions and the cathode surface, suggests that materials with more negative adsorption energies exhibit stronger metal ion-material affinity. This relationship is detailed through calculated adsorption energies (Figure 7k). Adsorption energy was calculated for two sites on each material (Figures S29 and S30, Supporting Information), identifying Bi_2O_2Se as having the highest adsorption capability, with Bi_2O_3 also effectively capturing Zn ions. In contrast, Bi_2Se_3 and Bi_2O_5Se showed weaker interactions with Zn ions. In addition, we also simulated the diffusion barriers of these materials to demonstrate the diffusion capabilities after adsorption on the material surface. As shown in Figure 7l, the energy barrier for Zn ion diffusion on the Bi_2O_5Se (100) surface is the lowest among these materials, while Bi_2Se_3 and Bi_2O_2Se exhibit similar but slightly higher diffusion barriers. Due to its non-layered structure and highly electronegative surface, Bi_2O_3 exhibits a much higher energy barrier than other materials. The supporting information for Figures S31–S34 (Supporting Information) show the molecular structure of the material along the stepwise diffusion path. Bi_2O_3 has a large diffusion barrier, which is much higher than other materials due to its strong adsorption. Bi_2O_5Se has the smallest Zn ion diffusion barrier due to the weak interaction with Zn ions. This represents that the greater the adsorption energy of Zn ions in the material, the more difficult it is to diffuse on the surface. Most importantly, similar diffusion barriers exist on the surfaces of Bi_2O_2Se and Bi_2Se_3, but Bi_2O_2Se has better Zn ion affinity compared to other materials. Accordingly, the electrochemical kinetics of Bi_2O_2Se would be the best in its adsorption and diffusion ability. The relationship between structural features and surface kinetics is displayed in Figure 7m. Excellent surface affinity and diffusion kinetics of Bi_2O_2Se can boost the performance of dual mechanisms with attractive capacity due to the high delivering number of electrons and Zn ions. Enhanced carrier mobility can promote capacity performance, and, more importantly, capacity retention. The low diffusion barrier enhances the easy transport of zinc ions within the internal material and reduces the overpotential during continuous cycling, thus reducing the diffusion resistance before and after cycling tests. High zinc ion affinity can promote structural activity in capturing zinc ions and their intermediates, driving stepwise Faradaic reactions and reversibility. Compared to layered materials, non-layered materials establish a high diffusion barrier for cations due to the lack of vdW gaps, abundant free electrons, and unbound electronegative atoms. In contrast, Bi_2O_2Se, with its electron-rich $[Se]^{2-}$ layer, improves cation surface affinity, enabling adsorption at active sites. At the same time, Bi_2O_2Se maintains its layered nature and exposed zipper-like layers that are not composed of the strong covalently bonded framework found in non-layered materials. The carrier mobility of the $[Bi_2O_2]$ conducting channel can effectively improve the dynamic behavior of carriers on highly electronegative surfaces. Therefore, it can easily achieve the highest capacity and highest electron transfer among these materials. The high carrier mobility is improved by a weak scattering effect under Se-poor condition, stabilizing the conducting channels and expediting solvated cations transported through the surface and interlayer. The electron conduction channels are located spatially away from ionized donor defects (Se vacancies) in different electrostatic layers. Se vacancies that are located in the Se layer are spatially separated from the conducting electrons. Consequently, spatial separation can strongly suppress the scattering caused by donor sites and subsequently increase the electron carrier mobility. However, when the Bi atoms in $[Bi_2O_2]$ layers are replaced by Se atoms, these Se atoms will scatter electrons strongly, since it distributes in the same $[Bi_2O_2]$ layer as the conduction band according to previous studies.[47]

According to above advantages, zipper-like Bi_2O_2Se with defect modulation possesses the electrochemical performances, including high Zn-ion-dominated capacity, long cycle life, high-current tolerance, and kinetic transport. Compared to other materials in previous literatures (**Figure 8**), both tunnel-type and non-layered materials (e.g., Bi_2O_3, MnO_2,[73] $Zn_xMo_{2.5}+yVO_{9+z}$,[74] $H_xV_2O_5$,[75] V_4O_9,[76] WO_3,[77]) own a stable structure for ion insertion, thereby delivering high-rate capability and reversibility. However, the structural limitations exhibit an obstacle for charge carrier accommodation, resulting in lower

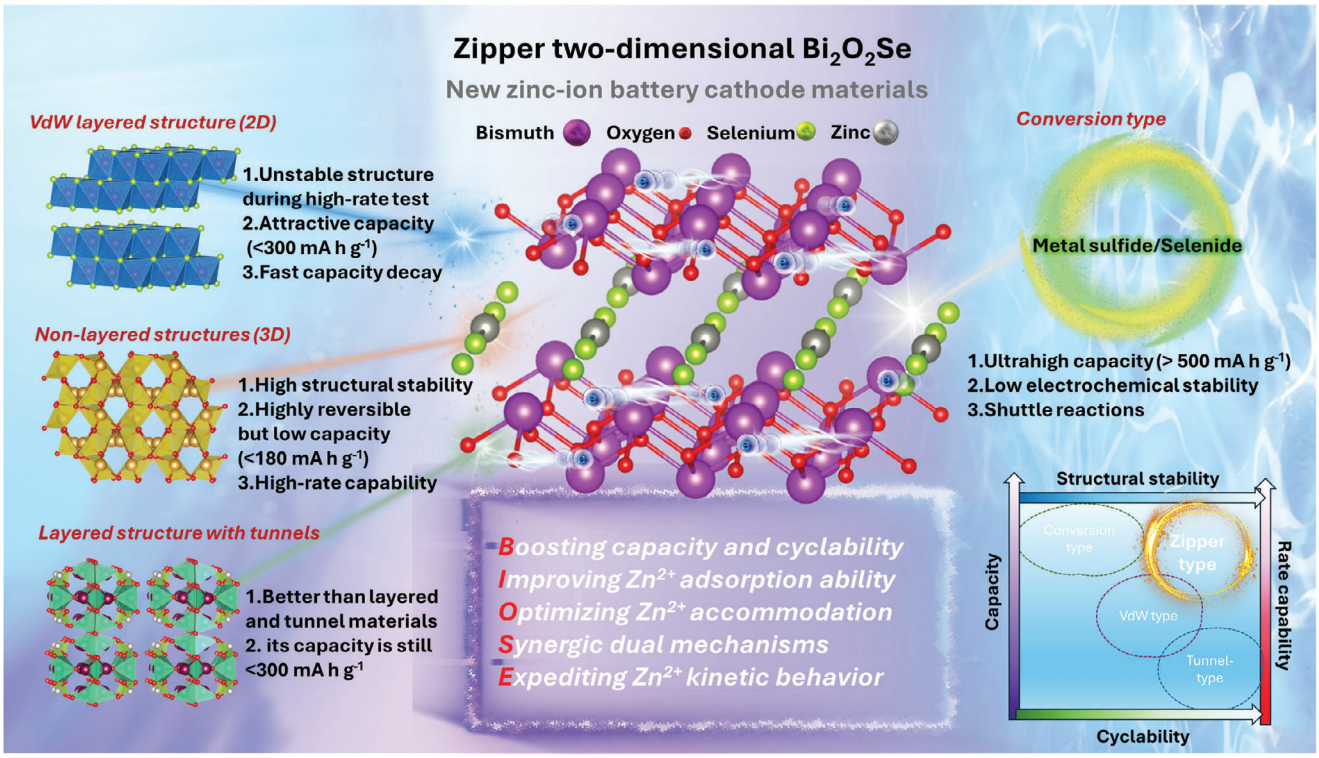

Figure 8. Schematic illustration of advantages and disadvantages of zipper 2D Bi_2O_2Se, vdW layered materials, non-layered materials, layered materials with tunnels, and conversion-type materials. On basis of structural stability, capacity, cyclability, and rate capability, the Bi_2O_2Se delivers the optimized performance compared with other materials.

capacities (< 200 mA h g^{-1}). The vdW layered materials (e.g., Bi_2Se_3, Bi_2O_5Se, (Na,Mn)V_8O_{20},[78] $VOPO_4$,[79,80] $Ni_3Mn_{0.7}Fe_{0.3}$-LDH,[81]) deliver a larger accommodation of charge carriers than tunnel/non-layered materials, thereby providing an attractive capacity (<300 mA h g^{-1}). The conversion-type materials such as metal chalcogenide and sulfur/selenium (e.g., Se@C,[82] Ru-doped Se,[83] S@CNTs-50,[84]) exhibit a ultrahigh capacity (>300 mA h g^{-1}) but low electrochemical and structural stability, leading to poor cyclability (<1000 cycles). In addition, layered Bi_2O_5Se showed a better cyclability compared to Bi_2Se_3 owing to its stable tunnel structure, and, therefore, it displayed a good cycling lifespan and rate capability than that of Bi_2Se_3. Importantly, zipper 2D Bi_2O_2Se as a novel cathode material in the ZIB system demonstrates an optimized electrochemical performance compared to these three types of cathode materials. First, its quasi-layered structure enables a high capacity from the redox current of insertion reactions. Zn ions inserted in electrostatic layers also react with Se atoms, facilitating a conversion reaction. This synergistic dual mechanism enhances Zn ion accommodation, resulting in the highest capacity among the materials in this study. Second, stable fluorite-like [Bi_2O_2] layers in Bi_2O_2Se are maintained across cycles, as confirmed by Operando XRD and SXRD, improving cyclability and redox reaction repeatability. Bi_2O_2Se, featuring [Bi_2O_2] conducting channels and electrostatic Se layers, combines layered structure with unique electronic properties, offering higher electron mobility than Bi_2Se_3, Bi_2O_5Se, and Bi_2O_3. This structural stability ensures the framework and Se layers persist post-discharge and charge, ensuring outstanding reversibility of insertion and conversion reactions across a range of current densities. Third, carrier mobility can be improved through the adjustment of Se content to induce deficient Se sites. Free electrons released from Se vacancies are automatically transferred to conducting channels due to donor levels of V_{Se} lied above the bottom of the conduction band in energy.[47] The increase of carrier density facilitates carrier mobility and conductivity, further enhancing the Zn-ion affinity and fast kinetic behavior. The simulation proved that the Bi_2O_2Se exhibited the highest adsorption energy with a low diffusion barrier, meaning that the Zn ions can more efficient and effective react with Bi_2O_2Se, which are confirmed by the low R_{ct} and Z_w during the cycling process. The low overpotential and voltage hysteresis verify the facile kinetic transfer and diffusion at each redox reaction. The Se-poor Bi_2O_2Se excels in capacity, cyclability, rate capability, and structural stability, exhibiting comprehensive benefits as a Zn-ion battery cathode.

3. Conclusion

Zipper-type Bi_2O_2Se structure merges quasi-layered traits with an active Se layer, effectively lowering charge transfer and diffusion resistances and showcasing a synergistic dual mechanism. Operando experiments and simulations confirm Bi_2O_2Se's enhanced electrochemical kinetics and reversibility in insertion and conversion reactions, offering a superior redox capacity over both layered and non-layered materials. Notably, Se content in Bi_2O_2Se's electrostatic layers significantly influences voltage plateau and capacity retention, driven by the covalent

framework's integrity and charge transfer enhancement from Se vacancies. Se-poor Bi_2O_2Se, with its increased carrier mobility and structural stability, outperforms Se-rich Bi_2O_2Se in capacity retention and rate durability. The difference stems from the enhanced electron transfer in $[Bi_2O_2]$ conducting channels, driven by the donor capacity of deficient sites in electrostatic layers. This, combined with the structural integrity of $[Bi_2O_2]$ framework, facilitates efficient Zn ion transport, reducing redox overpotentials, polarization, and voltage hysteresis.

The systematic movement of electron carriers enhances the passage of Zn ions through the $[Bi_2O_2]$ channels and electrostatic layers of Bi_2O_2Se. Even after long-term cycling, the electrochemical impedances of Bi_2O_2Se remain minimal compared to those of other cathodes. This study not only presents a strategy for unlocking high-performance cathode materials with unique structural characteristics and enhanced carrier mobility but also opens new avenues for thorough analysis of zipper-type materials in aqueous ZIBs.

Supporting Information

Supporting Information is available from the Wiley Online Library or from the author.

Acknowledgements

This work was supported by the financial support from the 2030 Cross-Generation Young Scholars Program by the National Science and Technology Council, Taiwan (NSTC 112-2628-E-007-016).

Conflict of Interest

The authors declare no conflict of interest.

Author Contributions

Y.-Y.H. performed conceptualization, methodology, and data curation, and wrote the final manuscript. Y.-C.C. performed data curation. H.-Y.T. performed conceptualization, acquired resources, supervised the project, and wrote, reviewed, and edited the final manuscript.

Data Availability Statement

The data that support the findings of this study are available from the corresponding author upon reasonable request.

Keywords

aqueous batteries, carrier mobility, quasi-layered, Se vacancy, zinc ion battery

Received: April 24, 2024
Revised: May 30, 2024
Published online:

[1] X. Tang, D. Zhou, B. Zhang, S. Wang, P. Li, H. Liu, X. Guo, P. Jaumaux, X. Gao, Y. Fu, *Nat. Commun.* **2021**, *12*, 2857.
[2] Y. Liang, H. Dong, D. Aurbach, Y. Yao, *Nat. Energy* **2020**, *5*, 646.
[3] Z. Pan, X. Liu, J. Yang, X. Li, Z. Liu, X. J. Loh, J. Wang, *Adv. Energy Mater.* **2021**, *11*, 2100608.
[4] X. Wang, Z. Zhang, B. Xi, W. Chen, Y. Jia, J. Feng, S. Xiong, *ACS Nano* **2021**, *15*, 9244.
[5] M. Zhang, R. Liang, T. Or, Y.-P. Deng, A. Yu, Z. Chen, *Small Structures* **2021**, *2*, 2000064.
[6] D. B. Kumar, W. Nie, Z. Jiang, J. Lee, T. Maiyalagan, *J. Alloys Compd.* **2023**, *960*, 170828.
[7] Y.-Y. Hsieh, H.-Y. Tuan, *Energy Storage Mater.* **2024**, *68*, 103361.
[8] W. Nie, H. Cheng, Q. Sun, S. Liang, X. Lu, B. Lu, J. Zhou, **2023**, *13*, 2201572.
[9] Y. Tian, Y. An, C. Wei, B. Xi, S. Xiong, J. Feng, Y. Qian, *Adv. Energy Mater.* **2021**, *11*, 2002529.
[10] Y. Ding, L. Yin, T. Du, Y. Wang, Z. He, J. A. Yuwono, G. Li, J. Liu, S. Zhang, T. Yang, *Adv. Funct. Mater.* **2024**, 2314388.
[11] J. Wan, R. Wang, Z. Liu, L. Zhang, F. Liang, T. Zhou, S. Zhang, L. Zhang, Q. Lu, C. Zhang, *ACS Nano* **2023**, *17*, 1610.
[12] X. Li, C. Cai, P. Hu, B. Zhang, P. Wu, H. Fan, Z. Chen, L. Zhou, L. Mai, H. J. Fan, *Adv. Mater.* **2024**, *36*, 2400184.
[13] M. Song, H. Tan, D. Chao, H. J. Fan, *Adv. Funct. Mater.* **2018**, *28*, 1802564.
[14] B. Tang, L. Shan, S. Liang, J. Zhou, *Energy Environ. Sci.* **2019**, *12*, 3288.
[15] M. Wang, J. Zhang, L. Zhang, J. Li, W. Wang, Z. Yang, L. Zhang, Y. Wang, J. Chen, Y. Huang, *ACS Appl. Mater. Interfaces* **2020**, *12*, 31564.
[16] Z. Yao, W. Zhang, X. Ren, Y. Yin, Y. Zhao, Z. Ren, Y. Sun, Q. Lei, J. Wang, L. Wang, *ACS Nano* **2022**, *16*, 12095.
[17] Y. Zong, H. Chen, J. Wang, M. Wu, Y. Chen, L. Wang, X. Huang, H. He, X. Ning, Z. Bai, *Adv. Mater.* **2023**, *35*, 2306269.
[18] J. Ding, H. Zheng, H. Gao, Q. Liu, Z. Hu, L. Han, S. Wang, S. Wu, S. Fang, S. Chou, *Adv. Energy Mater.* **2021**, *11*, 2100973.
[19] F. Wang, Z. Wang, T. A. Shifa, Y. Wen, F. Wang, X. Zhan, Q. Wang, K. Xu, Y. Huang, L. Yin, *Adv. Funct. Mater.* **2017**, *27*, 1603254.
[20] Y. Yang, X. Qiu, W. Shi, H. Hou, G. Zou, W. Huang, Z. Wang, S. Leng, Y. Ran, X. Ji, *Chem. Eng. J.* **2021**, *408*, 127247.
[21] Q. Liu, F. Zhan, X. Luo, Q. Yi, Z. Xiao, D. Zhai, J. Huang, Y. Zhang, H. Luo, D. Zhang, *Nano Energy* **2023**, *108*, 108252.
[22] X. Liu, Z. Zhang, Y. Wu, T. Wang, W. Wang, X. Su, D. Shi, H. Zhan, Y. Wang, *J. Environ. Chem. Eng.* **2024**, *12*, 111778.
[23] L.-D. Zhao, J. He, D. Berardan, Y. Lin, J.-F. Li, C.-W. Nan, N. Dragoe, *Energy Environ. Sci.* **2014**, *7*, 2900.
[24] Z. Wu, G. Liang, J. Wu, W. K. Pang, F. Yang, L. Chen, B. Johannessen, Z. Guo, *Adv. Energy Mater.* **2021**, *11*, 2100185.
[25] Y. Liang, X. Zhou, W. Li, H. Peng, *APL Mater.* **2021**, *9*, 060905.
[26] Y. Sun, J. Zhang, S. Ye, J. Song, J. Qu, *Adv. Funct. Mater.* **2020**, *30*, 2004480.
[27] C. Chen, M. Wang, J. Wu, H. Fu, H. Yang, Z. Tian, T. Tu, H. Peng, Y. Sun, X. Xu, *Sci. Adv.* **2018**, *4*, eaat8355.
[28] F. Wang, S. Yang, J. Wu, X. Hu, Y. Li, H. Li, X. Liu, J. Luo, T. Zhai, *InfoMat* **2021**, *3*, 1251.
[29] J. Wu, H. Yuan, M. Meng, C. Chen, Y. Sun, Z. Chen, W. Dang, C. Tan, Y. Liu, J. Yin, *Nat. Nanotechnol* **2017**, *12*, 530.
[30] Y. Sun, Z. Lian, Z. Ren, Z. Yao, Y. Yin, P. Huai, F. Zhu, Y. Huang, W. Wen, X. Li, *ACS Nano* **2021**, *15*, 14766.
[31] H. Yue, M. Han, X. Li, T. Song, Y. Pei, X. Wang, X. Wu, T. Duan, B. Long, *J. Colloid Interface Sci.* **2023**, *651*, 558.
[32] K. Zhu, T. Wu, S. Sun, W. van den Bergh, M. Stefik, K. Huang, *Energy Storage Mater.* **2020**, *29*, 60.
[33] Y. Sun, S. Ye, J. Zhang, J. Song, F. Zhou, J. Qu, *J. Mater. Chem. C* **2020**, *8*, 14711.
[34] W.-X. Yu, B. Liu, W.-Q. Huang, H. Zhou, S.-Y. Xie, *J. Phys.: Condens. Matter* **2022**, *35*, 075401.
[35] M. Zhang, M. Zhou, Z. Luo, J. Zhang, S. Wang, X. Wang, *Chem. Commun.* **2020**, *56*, 2558.

[36] Z. Li, K. Li, Y. Li, Y. Yu, J. Lv, X. Liu, K. Guan, W. Lei, S. Zhang, H. Zhang, *Adv. Funct. Mater.* **2024**, *34*, 2310371.
[37] X. Y. Zhang, D. Wang, Z. Zeng, C. Zhao, Y. Liu, B. Zhang, J. Pan, D. Liu, J. Wang, *J. Sol. Energy res.* **2022**, *9*, 1.
[38] M. Han, S. Wu, X. Zhao, Q. He, B. Zhang, W. Xiong, X. Luo, Y. Zheng, *Adv. Opt. Mater.* **2023**, *11*, 2300344.
[39] U. Khan, Y. Luo, L. Tang, C. Teng, J. Liu, B. Liu, H. M. Cheng, *Adv. Funct. Mater.* **2019**, *29*, 1807979.
[40] M. Yu, B. Ding, J. Wu, S. Zheng, X. Qian, L. Zhang, S. Zheng, L. Mao, J. Zhang, *Chem. Eng. J.* **2023**, *464*, 142586.
[41] D. Ling, Q. Wang, G. Tian, H. Yu, D. Zhang, Q. Wang, *ACS Nano* **2023**, *17*, 25222.
[42] Y.-Y. Hsieh, H.-Y. Tuan, *Energy Storage Mater.* **2022**, *51*, 789.
[43] M. Gao, W. Wei, T. Han, B. Li, Z. Zeng, L. Luo, C. Zhu, *ACS Appl. Mater. Interfaces* **2022**, *14*, 15370.
[44] X. Ren, X. He, X. Li, Y. Li, F. Gao, J. Zhang, P. Hu, *Adv. Opt. Mater.* **2024**, *12*, 2302852.
[45] W. Wang, Y. Meng, W. Wang, Z. Zhang, P. Xie, Z. Lai, X. Bu, Y. Li, C. Liu, Z. Yang, *Adv. Funct. Mater.* **2022**, *32*, 2203003.
[46] U. Khan, A. Nairan, K. Khan, S. Li, B. Liu, J. Gao, *Small* **2023**, *19*, 2206648.
[47] H. Fu, J. Wu, H. Peng, B. Yan, *Phys. Rev. B* **2018**, *97*, 241203.
[48] W. Hu, Y. He, Z. Yang, L.-C. Xu, L. Xue, R. Liu, X. Liu, *Appl. Surf. Sci.* **2024**, *652*, 159182.
[49] P. Li, A. Han, C. Zhang, X. He, J. Zhang, D. Zheng, L. Cheng, L.-J. Li, G.-X. Miao, X.-X. Zhang, *ACS Nano* **2020**, *14*, 11319.
[50] Q. Zhu, Q. Xiao, B. Zhang, Z. Yan, X. Liu, S. Chen, Z. Ren, Y. Yu, *J. Mater. Chem. A* **2020**, *8*, 10761.
[51] T. Chen, X. Zhu, X. Chen, Q. Zhang, Y. Li, W. Peng, F. Zhang, X. Fan, *J. Power Sources* **2020**, *477*, 228652.
[52] Y. Zhao, Y. Zhu, F. Jiang, Y. Li, Y. Meng, Y. Guo, Q. Li, Z. Huang, S. Zhang, R. Zhang, *Angew. Chem.* **2022**, *134*, e202111826.
[53] Y. Liao, H.-C. Chen, C. Yang, R. Liu, Z. Peng, H. Cao, K. Wang, *Energy Storage Mater.* **2022**, *44*, 508.
[54] Q. Lei, J. Zhang, Z. Liang, Y. Yue, Z. Ren, Y. Sun, Z. Yao, J. Li, Y. Zhao, Y. Yin, *Adv. Energy Mater.* **2022**, *12*, 2200547.
[55] J. Hao, L. Yuan, B. Johannessen, Y. Zhu, Y. Jiao, C. Ye, F. Xie, S. Z. Qiao, *Angew. Chem.* **2021**, *133*, 25318.
[56] Y. Bai, H. Zhang, B. Xiang, X. Liang, J. Hao, C. Zhu, L. Yan, *ACS Appl. Mater. Interfaces* **2021**, *13*, 23230.
[57] S. Deng, Z. Tie, F. Yue, H. Cao, M. Yao, Z. Niu, *Angew. Chem.* **2022**, *134*, e202115877.
[58] L. Wang, Z. Wu, M. Jiang, J. Lu, Q. Huang, Y. Zhang, L. Fu, M. Wu, Y. Wu, *J. Mater. Chem. A* **2020**, *8*, 9313.
[59] F. Tang, X. Wu, Y. Shen, Y. Xiang, X. Wu, L. Xiong, X. Wu, *Energy Storage Mater.* **2022**, *52*, 180.
[60] W. Xu, C. Sun, K. Zhao, X. Cheng, S. Rawal, Y. Xu, Y. Wang, *Energy Storage Mater.* **2019**, *16*, 527.
[61] H. Liu, J.-G. Wang, W. Hua, Z. You, Z. Hou, J. Yang, C. Wei, F. Kang, *Energy Storage Mater.* **2021**, *35*, 731.
[62] S. Zhang, C. Lin, J. Ye, D. Zhao, Y. Chen, J.-M. Zhang, J. Tao, J. Li, Y. Lin, S. F. Mertens, *Ceram. Int.* **2023**, *49*, 22160.
[63] Q. Wang, S. Wang, N. Wei, R. Wu, W. Zeng, L. Wen, Z. Chen, P. Gui, D. Liang, *Chem. Eng. J.* **2022**, *450*, 138132.
[64] Z. Lv, B. Wang, M. Ye, Y. Zhang, Y. Yang, C. C. Li, *ACS Appl. Mater. Interfaces* **2021**, *14*, 1126.
[65] Y. Y. Hsieh, H. Y. Tuan, *Small* **2023**, *19*, 2305342.
[66] A. M. Chaparro, C. Maffiotte, *Surf. Sci. Spectra* **2001**, *8*, 105.
[67] L. Ma, S. Chen, C. Long, X. Li, Y. Zhao, Z. Liu, Z. Huang, B. Dong, J. A. Zapien, C. Zhi, *Adv. Energy Mater.* **2019**, *9*, 1902446.
[68] A. L. Pereira, D. Santamaría-Pérez, J. Ruiz-Fuertes, F.-J. Manjón, V. P. Cuenca-Gotor, R. Vilaplana, O. Gomis, C. Popescu, A. Muñoz, P. Rodríguez-Hernández, *J. Phys. Chem. C* **2018**, *122*, 8853.
[69] M. Wang, G. Tan, D. Zhang, B. Li, L. Lv, Y. Wang, H. Ren, X. Zhang, A. Xia, Y. Liu, *Appl. Catal. B* **2019**, *254*, 98.
[70] M. Martin, A. Lasia, *Electrochim. Acta* **2011**, *56*, 8058.
[71] A. Dizon, C. You, M. E. Orazem, *Electrochim. Acta* **2021**, *391*, 138957.
[72] Y. Hu, Y.-Y. Wang, *IEEE Trans. Control Syst.* **2014**, *23*, 1180.
[73] Q. Chen, J. Jin, Z. Kou, C. Liao, Z. Liu, L. Zhou, J. Wang, L. Mai, *Small* **2020**, *16*, 2000091.
[74] W. Kaveevivitchai, A. Manthiram, *J. Mater. Chem. A* **2016**, *4*, 18737.
[75] J. Cao, D. Zhang, Y. Yue, T. Pakornchote, T. Bovornratanaraks, X. Zhang, Z. Zeng, J. Qin, Y. Huang, *ACS Appl. Mater. Interfaces* **2022**, *14*, 7909.
[76] Q. Wang, T. Sun, S. Zheng, L. Li, T. Ma, J. Liang, *Inorg. Chem. Front.* **2021**, *8*, 4497.
[77] G. Tian, Q. Wang, Z. Qu, H. Yu, D. Zhang, Q. Wang, *Small* **2023**, *19*, 2206701.
[78] M. Du, C. Liu, F. Zhang, W. Dong, X. Zhang, Y. Sang, J. J. Wang, Y. G. Guo, H. Liu, S. Wang, *Adv. Sci.* **2020**, *7*, 2000083.
[79] Z. Wu, C. Lu, F. Ye, L. Zhang, L. Jiang, Q. Liu, H. Dong, Z. Sun, L. Hu, *Adv. Funct. Mater.* **2021**, *31*, 2106816.
[80] K. Zhu, Z. Sun, P. Liu, H. Li, Y. Wang, K. Cao, L. Jiao, *J. Energy Chem.* **2021**, *63*, 239.
[81] Y. Zhao, P. Zhang, J. Liang, X. Xia, L. Ren, L. Song, W. Liu, X. Sun, *Adv. Mater.* **2022**, *34*, 2204320.
[82] C. Dai, L. Hu, H. Chen, X. Jin, Y. Han, Y. Wang, X. Li, X. Zhang, L. Song, M. Xu, *Nat. Commun.* **2022**, *13*, 1863.
[83] F. Cui, R. Pan, L. Su, C. Zhu, H. Lin, R. Lian, R. Fu, G. Zhang, Z. Jiang, X. Hu, *Adv. Mater.* **2023**, *35*, 2306580.
[84] W. Li, K. Wang, K. Jiang, *Adv. Sci.* **2020**, *7*, 2000761.